Theoretical advantages of a triaxial optically pumped magnetometer magnetoencephalography system

Matthew J. Brookes [a,*], Elena Boto [a], Molly Rea [a], Vishal Shah [b], James Osborne [b], Niall Holmes [a], Ryan M. Hill [a], James Leggett [a], Natalie Rhodes [a], Richard Bowtell [a]

[a] *Sir Peter Mansfield Imaging Centre, School of Physics and Astronomy, University of Nottingham, University Park, Nottingham NG7 2RD, United Kingdom*
[b] *QuSpin Inc., 331 South 104th Street, Suite 130, Louisville, CO 80027, United States*

ARTICLE INFO

ABSTRACT

The optically pumped magnetometer (OPM) is a viable means to detect magnetic fields generated by human brain activity. Compared to conventional detectors (superconducting quantum interference devices) OPMs are small, lightweight, flexible, and operate without cryogenics. This has led to a step change in instrumentation for magnetoencephalography (MEG), enabling a "wearable" scanner platform, adaptable to fit any head size, able to acquire data whilst subjects move, and offering improved data quality. Although many studies have shown the efficacy of 'OPM-MEG', one relatively untapped advantage relates to improved array design. Specifically, OPMs enable the simultaneous measurement of magnetic field components along multiple axes (distinct from a single radial orientation, as used in most conventional MEG systems). This enables characterisation of the magnetic field vector at all sensors, affording extra information which has the potential to improve source reconstruction. Here, we conduct a theoretical analysis of the critical parameters that should be optimised for effective source reconstruction. We show that these parameters can be optimised by judicious array design incorporating triaxial MEG measurements. Using simulations, we demonstrate how a triaxial array offers a dramatic improvement on our ability to differentiate real brain activity from sources of magnetic interference (external to the brain). Further, a triaxial system is shown to offer a marked improvement in the elimination of artefact caused by head movement. Theoretical results are supplemented by an experimental recording demonstrating improved interference reduction. These findings offer new insights into how future OPM-MEG arrays can be designed with improved performance.

1. Introduction

Magnetoencephalography (MEG) is the measurement of the magnetic fields generated at the scalp by current flow through neuronal assemblies in the brain (Cohen, 1968). Mathematical modelling of these fields (termed source reconstruction) enables the generation of 3D images showing moment-to-moment changes in neural current flow. In this way, MEG offers a unique non-invasive window on brain function, enabling us to track activity within (and connectivity between) brain regions in real time, as those regions become engaged to support cognition (Baillet, 2017). This provides a powerful tool for basic neuroscience and a useful clinical metric, particularly in disorders like epilepsy (Rampp et al., 2019) which involve abhorrent electrophysiology.

The magnetic fields generated by brain activity are small – of order 100 fT – and until recently the only viable tool for their measurement was the superconducting quantum interference device (SQUID)

(Jaklevic et al., 1964; Zimmerman et al., 1970; Cohen, 1972). In most MEG systems, a superconducting pick-up coil is placed close to the scalp, and orientated to measure the "radial" (perpendicular to the scalp) component of neuromagnetic field. Each pick-up coil is inductively coupled to a SQUID, which exploits quantum interference and a calibrated feedback loop to measure magnetic field changes through the pick-up coil, with a noise level between 2 and 10 fT/sqrt(Hz). Around 300 separate pick-up coils and SQUIDs surround the head, and this array allows measurement of electrical brain activity with millisecond temporal precision (Hamalainen et al., 1993). Following source reconstruction, images of changing neural current can be generated with spatial precision of a few millimetres (Barratt et al., 2018).

These systems prove extremely effective for functional neuroimaging. However, the requirement for cryogenics limits their utility. Since both the pick-up-coil and SQUID must be housed in a cryogenic vessel, the sensor array is rigid, and one-size-fits-all. This means that there can be no adaptability for different head sizes, resulting in inhomogeneous

---

and sometimes poor spatial coverage. A thermally insulating gap must be maintained between the scalp and the pick-up coils, which moves the coils away from the head, reducing signal strength (in accordance with an inverse square law). Because the array is fixed, movement of the participant during a scan results in a degradation of data quality. Finally, cryogenic infrastructure makes MEG systems complex and expensive. For these reasons, the uptake of MEG, particularly clinically, has remained limited.

In recent years, the MEG field has been changed fundamentally by the introduction of a new generation of quantum-enabled magnetic field sensors. Optically pumped magnetometers (OPMs) offer field sensitivity similar to that of SQUIDs (noise levels ~7–15 fT/sqrt(Hz)) without the requirement for cryogenic cooling (Allred et al., 2002; Kominis et al., 2003). Miniaturisation has allowed OPMs to be made small and lightweight (Allred et al., 2002; Kominis et al., 2003; Mhaskar et al., 2012; Sander et al., 2012; Johnson et al., 2013; Shah and Wakai, 2013; Kamada et al., 2015; Sheng et al., 2017), making them perfect for MEG. Many studies have shown the suitability of OPMs for the detection of neuromagnetic fields (e.g. Xia et al., 2006; Johnson et al., 2010; Sander et al., 2012; Kamada et al., 2015; Boto et al., 2017)), and nascent systems incorporate up to ~50 sensors integrated into a lightweight helmet which can be mounted on a subject's head (e.g. (Hill et al., 2020; Boto et al., 2021)). Sensor mounting can be flexible, meaning that different head shapes and sizes can be accommodated (Hill et al., 2019). Moreover, assuming that the background magnetic field is controlled (Holmes et al., 2018; Holmes et al., 2019b), MEG data can be acquired whilst a subject makes large movements (Boto et al., 2018). This offers a step change in the utility of MEG; data acquisition in individuals who would not fit in a conventional system (e.g. babies) or who would find it challenging to remain still (e.g. patients with movement disorders) is possible. Likewise a wearable system enables new possibilities for neuroscientific study, for instance allowing brain activity to be measured whilst subjects are immersed in virtual reality (Roberts et al., 2019) or undertaking naturalistic tasks (Hill et al., 2019). In addition, because sensors are closer to the brain (as no insulating gap is required), OPM-MEG systems offer higher sensitivity, and improved spatial resolution (Boto et al., 2016; Iivanainen et al., 2017; Boto et al., 2019).

Many of the advantages of OPMs have been demonstrated. However, one untapped area relates to the flexibility of design. Most conventional systems use inductive sensors that measure field along a single orientation. For this reason, the neuromagnetic field is usually measured on the radial axis. However, OPMs work in a fundamentally different way (see (Tierney et al., 2019) for a review). In brief, an OPM contains a vapour of alkali atoms whose atomic spins are aligned through optical pumping. This alignment gives the vapour a bulk magnetic property which can be altered by the presence of an external magnetic field, according to the Bloch equations (Shah and Romalis, 2009). By monitoring how the strength of the laser beam is modulated as it passes through the vapour, it is possible to gain very sensitive magnetic field measures. This design offers significant flexibility. For example, existing solutions allow measurement of field components in multiple orientations (Borna et al., 2020). Further refinement (e.g. splitting the laser beam and sending two beams through the same cell, or using two different modulation frequencies) offer the possibility of measuring the full (3D) field vector. Even using single axis sensors, their lightweight and flexible nature enables easy placement to measure field at different orientations. This allows new types of sensor array to be conceived. Iivanainen et al. (Iivanainen et al., 2017) simulated both dual axis and triaxial sensor arrays, showing them to offer greater information content relating to the neuromagnetic field (and higher overall signal amplitude) compared to the use of radial sensors. This extra information should provide improved characterisation of neuromagnetic fields, and consequently (assuming source localisation methods are able to exploit this information) neuronal signals.

Here, we investigate how an array comprised of flexibly placed triaxial OPMs might behave when source localisation via a beamformer

spatial filter (a popular source reconstruction algorithm (Robinson and Vrba, 1998)) is applied. Specifically, we hypothesise that a system comprising 'triaxial' OPMs will offer more accurate source reconstruction, particularly in the presence of external magnetic interference. The article is split into three sections. In Section 1, we describe a MEG beamformer, and via analytical assessment, determine the parameters of MEG array design that will affect its ability to reconstruct high fidelity signals. We then explore how these parameters are affected by triaxial measurement. In Section 2, we confirm our analytical insights via simulations that show how a triaxial array will behave in the presence of interference and subject movement. Finally, in Section 3, using a model of triaxial measurement in which a small number of (single axis) OPMs are rotated, we test experimentally the triaxial theory and its effect on real external interference.

2. Theory

Throughout this paper, we will consider three hypothetical MEG sensor arrays: 1) A 50 sensor system with radially orientated sensors (Fig. 1A). 2) A 50 sensor triaxial system in which each sensor offers three orthogonal measurements of magnetic field (meaning 150 channels in total) (Fig. 1B). 3) A 150-channel radial only system (Fig. 1C). In all three cases we assume that the sensors are uniformly distributed over the surface of a hemisphere (of radius 8.6 cm). For the triaxial system, sensors are orientated to measure magnetic field in the radial (e_r), polar (e_θ) and azimuthal (e_ϕ) orientations.

2.1. The beamformer spatial filter

Source reconstruction is the process of deriving 3D images of electrical activity in the brain from measured magnetic field data. To understand how source reconstruction (and consequently MEG results) might differ across different designs of sensor array, we will use a beamformer approach (Robinson and Vrba, 1998). Using a beamformer, the electrical activity, $\hat{q}_\theta(t)$, at some location and orientation, θ, in the brain is reconstructed based on a weighted sum of sensor measurements such that

$$\hat{q}_\theta(t) = \boldsymbol{w}_\theta^T \boldsymbol{b}(t), \tag{1}$$

where $\boldsymbol{b}(t)$ is a vector of MEG data acquired across N channels at time t, and the 'hat' notation denotes a beamformer estimate of the true activity, $q_\theta(t)$. $\boldsymbol{w}_\theta^T$ are the weighting coefficients which would ideally be derived to ensure that any electrical activity originating at θ is maintained in the estimate, and all other activity suppressed. To do this, we minimise the variance of the estimate (i.e. $E((\hat{q}_\theta(t))^2)$) subject to the linear constraint that source power originating at θ must remain. Mathematically,

$$min_{\boldsymbol{w}_\theta} E\left(\left(\hat{q}_\theta(t)\right)^2\right) \ subject \ to \ \boldsymbol{w}_\theta^T \boldsymbol{l}_\theta = 1, \tag{2}$$

where $\boldsymbol{l}_\theta$ is a model of the magnetic fields that would be recorded if there were a current dipole at θ with unit amplitude (i.e. $\boldsymbol{l}_\theta$ is the forward model). $E(x)$ denotes expectation value. The solution to this is

$$\boldsymbol{w}_\theta^T = \frac{\boldsymbol{l}_\theta^T \boldsymbol{C}^{-1}}{\boldsymbol{l}_\theta^T \boldsymbol{C}^{-1} \boldsymbol{l}_\theta}, \tag{3}$$

where $\boldsymbol{C}$ is the data covariance matrix.

2.2. A single source with uncorrelated Gaussian sensor noise

2.2.1. Analytical breakdown

For the purposes of this paper, we want to know the error between the beamformer estimate ($\hat{q}_\theta(t)$) and the true source timecourse ($q_\theta(t)$) and how this is impacted by array design. We start with the simplest possible case, where MEG data contain activity from a single source
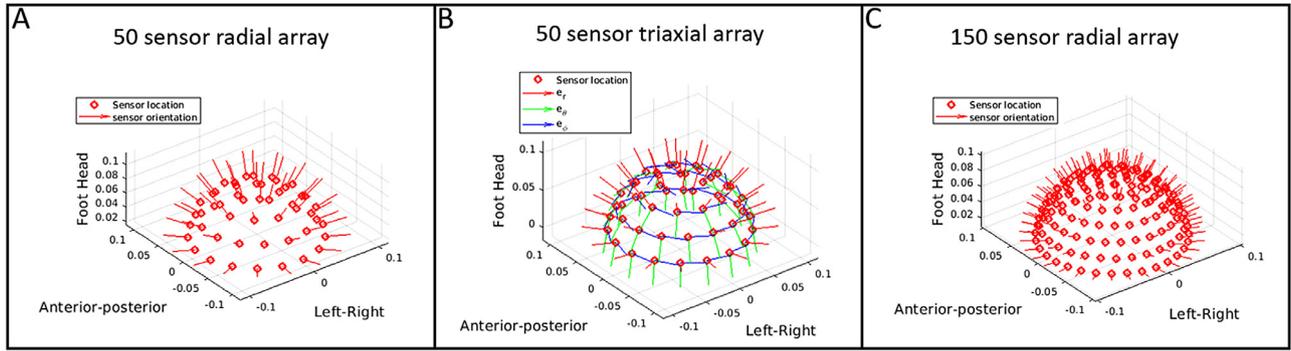
Fig. 1. Three hypothetical MEG systems. A) 50-sensor (and 50 channel) radial array. B) 50 sensor (150 channel) triaxial array. C) 150 sensor (150 channel) radial array. The circles show the sensor locations and the lines show the orientation along which field is measured.

in the brain, with timecourse $q(t)$, and additive random noise at each sensor, $e(t)$. Here, the MEG data can be expressed as

$$b(t) = lq(t) + e(t), \tag{4}$$

where l is the forward field for the single source. We next assume that we use the beamformer to focus on the true location of the source, and that the source model is accurate (i.e. $l_\theta \to l$). We also use an analytical form for the data covariance matrix (i.e. we assume that the data covariance matrix is a "perfect" representation) Brookes et al., 2008). In this case, a substitution of Eqs. (3) and (4) into Eq. (1) (see Appendix A) allows us to write that

$$\hat{q}(t) = q(t) + \frac{1}{\|l\|^2} l^T e(t), \tag{5}$$

where $\|l\|$ is the Frobenius norm of the forward field vector, l. Here, the first term shows that the source estimate contains a true representation of the source timecourse. The second term shows that, for each time point, the reconstructed data are contaminated by a projection of the sensor noise through the forward field.

Eq. (5) only represents a single point in time and a more useful metric involves the summed square of the error across the reconstructed timecourse, which can be written

$$E_{tot} = \frac{1}{\sqrt{M}} \sqrt{\sum_{i=1}^{M} (\hat{q}_i - q_i)^2}, \tag{6}$$

where M is the total number of time points in the recording. Mathematically, we can show (see Appendix A) that this total error in the beamformer reconstruction collapses to the convenient expression

$$E_{tot} = \frac{v}{\|l\|}. \tag{7}$$

v is the standard deviation of the noise at each sensor, which we assume is equal across sensors and is an inherent property; i.e. we shall assume it to be fixed (at around 10 fT/Sqrt(Hz) for OPMs). $\|l\|$ is a measure of how the sensor array is affected by the source, and it follows that, to minimise the overall error in the beamformer projected timecourse, we must design an array to maximise $\|l\|$.

2.2.2. Simulation of the forward field norm

To investigate how $\|l\|$ behaves across different array configurations we calculated the magnetic field, l_i, generated by a 1 nAm source in the brain at each sensor location/orientation, i. For each i, l_i was calculated at the sensor locations as the dot product of the field vector with the sensitive axis (or axes). This was done independently for each of the arrays in Fig. 1. The field was calculated based on the derivation by Sarvas (Sarvas, 1987), assuming the head to be a spherically symmetric homogeneous conductor and that brain activity can be approximated as a current dipole. $\|l\|$ computed as $\|l\| = \sqrt{\sum_{i=1}^{N} l_i}$, where N is the number

of channels (i.e. 50 for the system in Fig. 1A; 150 for the systems in Fig. 1B and 1C). Note that, for the triaxial system, l is the concatenation of fields for the three orientations (i.e. $l = [l_{radial}, l_{polar}, l_{azimuth}]$) whereas for the other two systems only radial fields are considered.

This calculation was run 6000 times, with the dipole at a different locations/orientations on each run. For each of the systems, we averaged $\|l\|$ over all realisations; we also computed the average (over realisations) of $\|l_{radial}\|$ and $\|l_{azimuth}\|$. E_{tot} was computed (as in Eq. (7)) as a function of $\|l\|$ (concatenating values over all systems) to show how the overall beamformer projected error behaves.

For completeness, for radial sensors we looked at how $\|l\|$ varies with sensor count. An algorithm was used to place between 31 and 325 sensors equidistantly on a hemispherical surface. For each sensor count, we simulated 25 source locations and computed the average value of $\|l\|$. This was in order to derive, approximately, how $\|l\|$ for a 150 channel triaxial system compares to $\|l\|$ for radial only arrays.

Fig. 2A shows an example forward field computed at each of the 50 sensors for the triaxial system. Fig. 2B shows a visual representation of the same example on a flattened representation of the head; the left hand map shows the distribution of radially oriented field, whilst the centre-left and centre-right maps show the polar and azimuthal fields. For comparison, the forward field for a 150-channel radial system is also shown on the right. Note that, for the tangential orientations (polar and azimuth) there is a significant departure from the 'classical' dipolar field pattern which is well known in MEG. Although these fields have been calculated using a simple model, they are visually similar to measured tangential fields in previous MEG studies (Haueisen et al., 2012; Borna et al., 2020).

Fig. 2C shows the variation of total error in a beamformer reconstruction with the norm of the forward field. Each point represents a different realisation of the forward field simulation; values for the 50 channel radial system are shown in blue, the 150 channel triaxial system in red, and the 150 channel radial system in green. The curve shows that (for this simple model) the 150 channel radial system offers the lowest beamformer reconstruction error. Fig. 2D shows the mean $\|l\|$ value across all realisations of source location, for radial, tangential, triaxial and 150 channel radial systems. Notice that, in agreement with Iivanainen et al. (Iivanainen et al., 2017), $\|l\|$ is lower for the tangential orientations than for the radial orientation. Consequently, $\|l\|$ for a 50-sensor triaxial system (with 150 channels) tends to be higher than for a 50-channel radial system (as one would expect given the increased channel count), but not as high as for a 150-channel radial only system.

Fig. 2E shows how $\|l\|$ varies with channel count for a radial only system. The shaded area indicates standard deviation across dipole locations). As expected $\|l\|$ increases approximately monotonically with sensor count (the discontinuities are due to the way in which the algorithm placed the sensors on the sphere). For comparison we show the mean of $\|l\|$ for a 50-sensor radial array (blue), and a 50-sensor triaxial
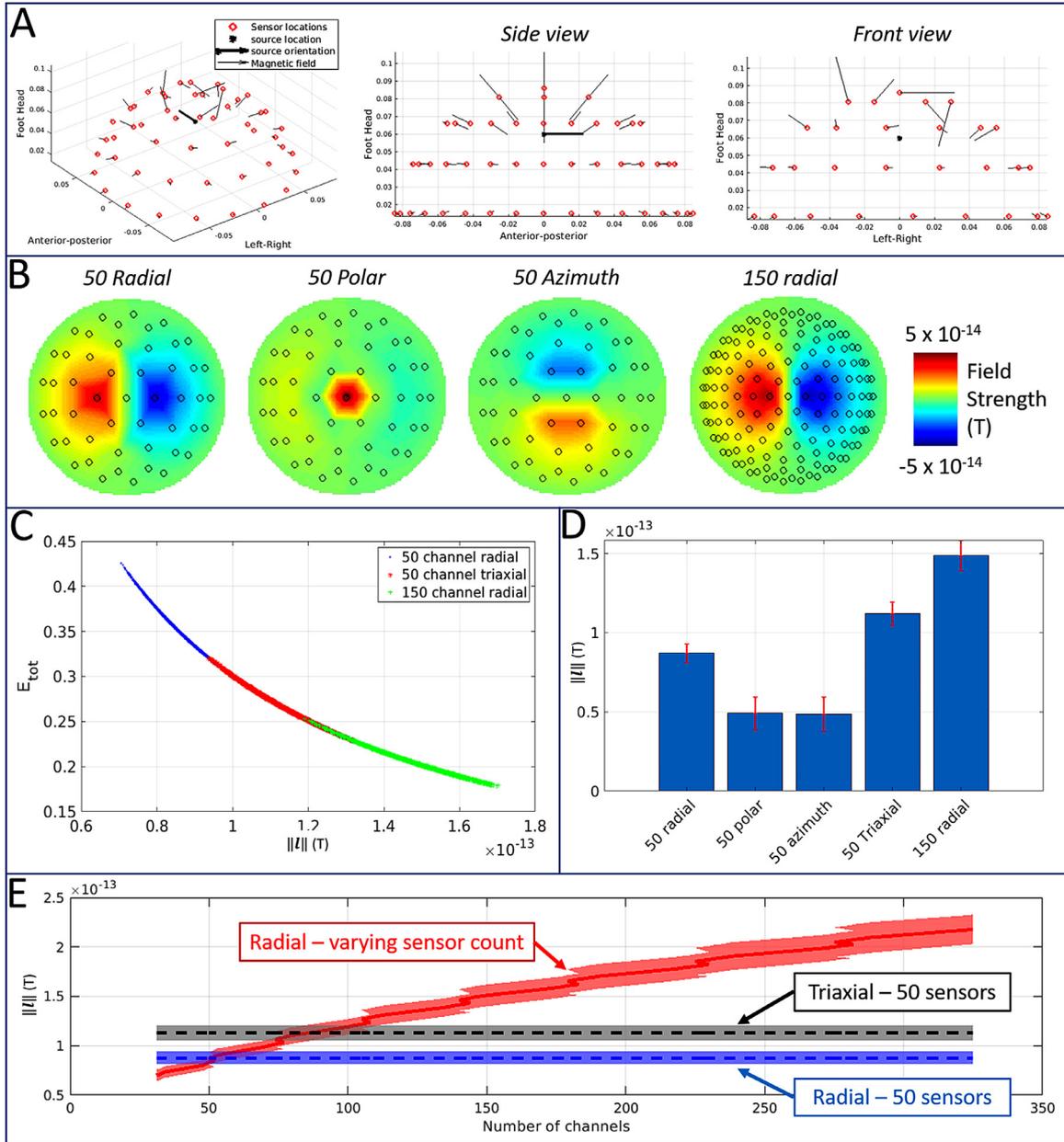
Fig. 2. Single source and sensor noise: A) vector magnetic fields generated by a single source with 1nAm amplitude. The same fields are shown viewed from three separate orientations. B) Field maps showing a different representation of the fields in (A). The left-hand map shows the fields projected along the radial direction; centre left shows the fields orientated along the polar axis; centre right shows fields orientated along the azimuthal axis. The right-hand map shows radial fields for a 150-channel radial system. C) Variation of total error in a beamformer reconstruction with the norm of the forward field. The curve follows the relationship in Eq. (7). Blue, red and green show results for the 50 channel radial, triaxial, and 150 channel radial systems, respectively. D) Bar chart showing mean of the norms (error bars show standard deviation) across separate source locations. E) The red curve shows how the norm of the forward field changes with sensor count for a radially-orientated sensor MEG system. For comparison, the black dotted line shows the forward field norm for a 50 channel triaxial system. The blue dotted line shows the forward field norm for a 50-channel radial system. (For interpretation of the references to colour in this figure legend, the reader is referred to the web version of this article.)

array (black). Based on this, $\|\boldsymbol{l}\|$ for the triaxial system is approximately equal to that for an 80-channel radial system.

2.3. Two sources with uncorrelated Gaussian sensor noise

2.3.1. Analytical breakdown

The analysis above is oversimplified because, generally, there is more than one "active" source contributing to the measured magnetic field. It therefore proves instructive to examine a mathematical model with two active sources. We assume that source 1 – with timecourse $q_1(t)$ and forward field $\boldsymbol{l}_1$ – is our source of interest in the brain, whereas source 2 - with timecourse $q_2(t)$ and forward field $\boldsymbol{l}_2$ – represents interference (e.g. a source outside the brain). In this scenario, the MEG data, $\boldsymbol{b}(t)$, are given by

$$\boldsymbol{b}(t) = \boldsymbol{l}_1 q_1(t) + \boldsymbol{l}_2 q_2(t) + \boldsymbol{e}(t) \tag{8}$$

where again $\boldsymbol{e}(t)$ contains the sensor errors. As before we assume that we reconstruct a source at the true location and orientation of source 1 so that,

$$\hat{q}_1(t) = \boldsymbol{w}_1^T \big(\boldsymbol{l}_1 q_1(t) + \boldsymbol{l}_2 q_2(t) + \boldsymbol{e}(t) \big) = q_1(t) + \boldsymbol{w}_1^T \boldsymbol{l}_2 q_2(t) + \boldsymbol{w}_1^T \boldsymbol{e}(t). \tag{9}$$

Note that, as with Eq. (5), the estimate of the timecourse of source 1 ($\hat{q}_1(t)$) again contains the true source's timecourse ($q_1(t)$), but now with two sources of error. For convenience we rewrite Eq. (9) as

$$\hat{q}_1(t) = q_1(t) + \delta q_2(t) + \epsilon(t), \tag{10}$$

and it is easy to see that the term $\delta q_2(t)$ represents interference from source 2 whilst ϵ is the error introduced by sensor noise. In designing a MEG array we must aim to minimise both terms.

Again by exploiting a mathematical formulation of the data covariance matrix (Brookes et al., 2008) (see Appendix B) it becomes possible to show that

$$\delta = \frac{\|l_2\|}{\|l_1\|} r_{12} \left[\frac{1 - f_2}{1 - f_2 r_{12}^2} \right], \tag{11}$$

where

$$r_{12} = \frac{l_1^T l_2}{\|l_1\|\|l_2\|} \tag{12}$$

is a measure of the similarity of the lead field patterns for sources 1 and 2. Geometrically this quantity represents the cosine of the angle between the vectors l_1 and l_2. Statistically it is related to the Pearson correlation coefficient between the two forward fields; i.e. if sources 1 and 2 were completely inseparable ($l_1 = l_2$) then $r_{12} = 1$. If l_1 and l_2 look completely different (e.g. as might be the case if sources 1 and 2 were both brain sources on opposite sides of the head) then $r_{12} = 0$. Note in this latter case, the interference from source 2 falls to zero. (r_{12} is similar to the lead field correlation metric used in a previous study (Iivanainen et al., 2017).) The quantity f_2 represents a scaled signal to sensor-noise ratio and is given by

$$f_2 = \frac{Q_2^2 \|l_2\|^2}{v^2 + Q_2^2 \|l_2\|^2}, \tag{13}$$

where Q_2 is the standard deviation of $q_2(t)$ across the duration of the MEG recording. Note that for very high signal to noise ratio, $f_2 \to 1$ and for very low signal to noise ratio $f_2 \to 0$. Eq. (11) is important since it tells us how a beamformer separates two sources. It governs spatial resolution (Barratt et al., 2018) (i.e. our ability to separate multiple sources in the brain) and it also highlights the advantages of beamforming over, e.g. a dipole fit (see Appendix D).

It is also possible to derive an expression for the error on the signal due to sensor noise by using a similar mathematical approach. Specifically, we can show (see Appendix B) that

$$\epsilon(t) = \frac{v}{\|l_1\|} \left[r_{1e}(t) \left(\frac{1}{1 - f_2 r_{12}^2} \right) - r_{2e}(t) \left(\frac{f_2 r_{12}}{1 - f_2 r_{12}^2} \right) \right] \tag{14}$$

where $r_{1e}(t) = \frac{l_1^T e(t)}{\|l_1\| v}$ denotes spatial correlation between the forward field of source 1, and the noise pattern. Similarly $r_{2e}(t) = \frac{l_2^T e(t)}{\|l_2\| v}$ denotes spatial correlation between the forward field of source 2, and the sensor noise.

This analytical description of additive noise on a beamformer reconstruction is only valid for a single time point and so, as previously, it is useful to quantify the total error across an entire timecourse. To do this we again use the sum of the squared difference between the reconstructed and original timecourse, thus

$$E_{tot}^2 = \sum_{i=1}^{M} (\hat{q}_{1i} - q_{1i})^2 \tag{15}$$

where i denotes the time point. As shown in Appendix B, assuming that sensor noise and both sources are temporally independent, we can write that the total error on the timecourse (E_{tot}^2) is given by the sum of the error from source 2, and the error from sensor noise, thus

$$E_{tot}^2 = E_{source}^2 + E_{noise}^2 \tag{16}$$

where

$$E_{source}^2 = \frac{Q_2^2 \|l_2\|^2}{\|l_1\|^2} r_{12}^2 \left[\frac{1 - f_2}{1 - f_2 r_{12}^2} \right]^2 \tag{17}$$

and

$$E_{noise}^2 = \frac{v^2}{\|l_1\|^2} \left(\frac{1 + f_2^2 r_{12}^2 - 2 f_2 r_{12}^2}{\left(1 - f_2 r_{12}^2\right)^2} \right). \tag{18}$$

Notice that in the case where either source 2 does not exist ($f_2 = r_{12} = 0$) or where the two sources are separable ($r_{12} = 0$) then the interference from the second source collapses to zero, and $E_{noise}^2 = \frac{v^2}{\|l_1\|^2}$.

The above analysis shows that, at least in theory, beamformer accuracy is governed by a relatively small number of parameters; some of those parameters are invariant to system design – e.g. Q_1 is set by the brain; Q_2 by the nature of the interference; v is inherent to the OPM design. However, other parameters can be altered by the way in which the array is structured. For example, $\|l_1\|$ and $\|l_2\|$ will both increase with channel count; and as we have seen in Fig. 2, $\|l_1\|$ will typically be larger for radially orientated sensors. Likewise, the correlation of field topographies (r_{12}) may be altered by judicious array design. For this reason, an understanding of Eqs. (17) and (18) becomes important for understanding how these parameters relate to overall MEG reconstruction accuracy.

Fig. 3 provides visualisations of Eqs. (17) and (18). We have assumed that $\|l_1\|$ and $\|l_2\|$ take a realistic range of values for the three systems in Fig. 1 and r_{12} was allowed to vary between 0 and 1. The sensor noise, v, was set to 100 fT and both source amplitudes (Q_1 and Q_2) were set to 1 nAm. The left, centre and right columns show the errors from source interference, sensor noise, and total error respectively. The upper row shows how error behaves when varying $\|l_1\|$ and r_{12}. The middle row shows error variation versus $\|l_2\|$ and r_{12}. Finally, the lower row shows error versus $\|l_1\|$ and $\|l_2\|$.

According to this theoretical model, the two most important parameters for minimising total beamformer error are $\|l_1\|$ and r_{12}; if a system can be optimised such that r_{12} is minimised, whilst $\|l_1\|$ is maximised, this can result in a huge reduction in overall error. Note that, for a fixed value of r_{12}, error decreases monotonically with increasing $\|l_1\|$ and varying $\|l_2\|$ has relatively little effect.

2.3.2. Triaxial measurement and r_{12}

To understand how r_{12} relates to array design we undertook a final calculation. Using a model of a current dipole in a conducting sphere (Sarvas, 1987), we measured how r_{12} changes given the three different systems shown in Fig. 1. On each iteration of this calculation we simulated one source of interest in the brain, and one source of interference. Brain sources were simulated at a depth of between 2 cm and 2.4 cm from the sphere surface with (randomised) tangential orientation. We simulated two types of interference source: First, we considered an internal source, which comprised a current dipole within the conducting sphere. This would model a second source (of no interest) in the brain. The distance between the source of interest and interference source was derived from a uniform distribution, and was between 20 and 60 mm. The orientation of the second source was also tangential. Second, we simulated a source of interference external to the brain. For convenience, external sources were also taken to be current dipoles and were located between 0.2 m and 0.6 m from the centre of the sphere. (Note that, for these distances, the fields generated by these current dipoles would be approximately equivalent to those from a magnetic dipole.) For both internal and external interference we measured r_{12}. 25,000 iterations of this calculation were run with the source locations changing on each iteration.

Fig. 4A shows r_{12} values averaged over iterations for internal (left) and external (right) interference sources. Whilst for internal interference, the improvement offered by a triaxial system is modest, for external interference the improvement is dramatic. The reason for this is
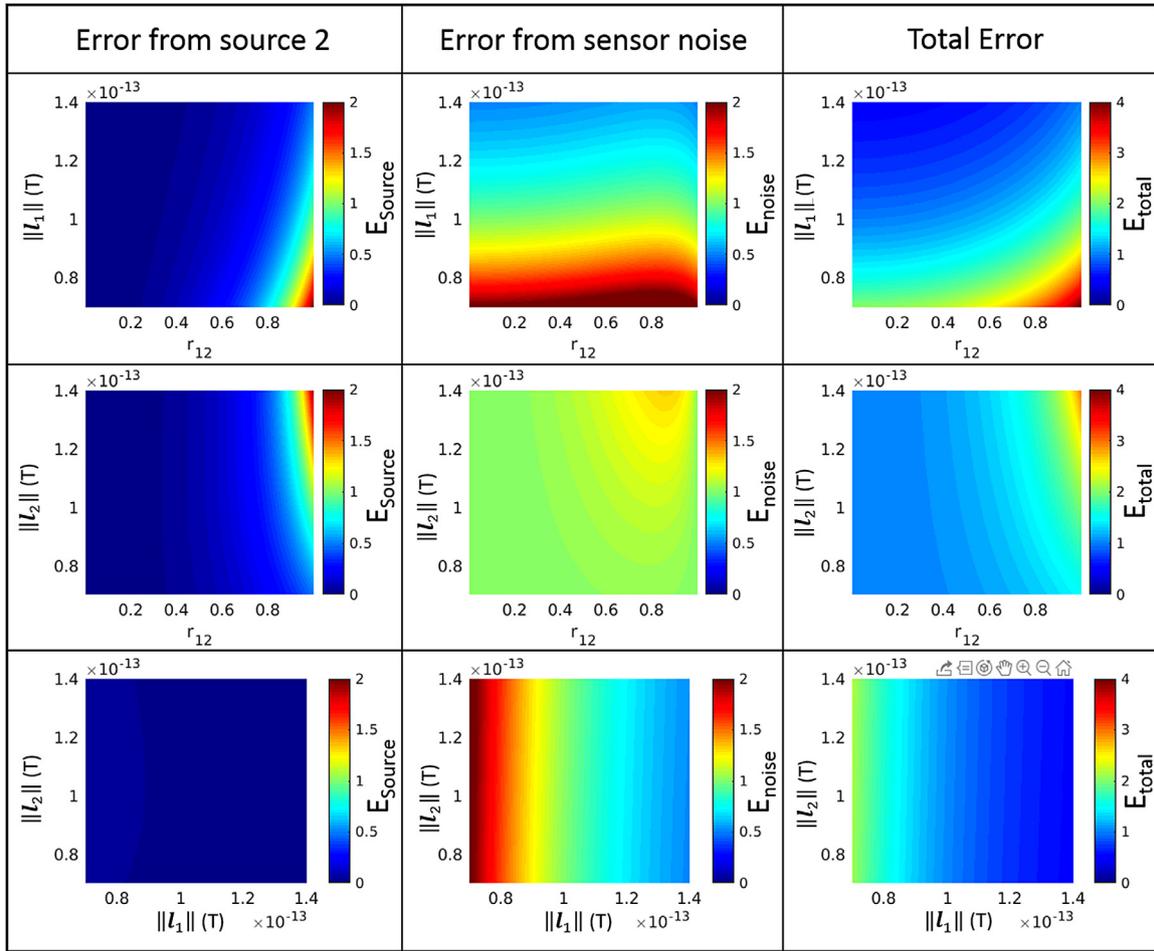
Fig. 3. Theoretical analysis of the errors in beamformer reconstruction. We have assumed a simple model of two sources (1 and 2, with source two representing unwanted interference) and uncorrelated sensor noise. The left, centre and right columns show interference from source two, sensor noise, and total error respectively. The upper row shows error as a function of $\|l_1\|$ and r_{12} (with $\|l_2\|$ set to 1×10^{-13} T). The middle row shows error versus $\|l_2\|$ and r_{12} (with $\|l_1\|$ set to 1×10^{-13} T). The lower row shows error versus $\|l_1\|$ and $\|l_2\|$ (with r_{12} set to 0.5). Sensor noise was assumed to be $\nu = 100$ fT and both source amplitudes were 1 nAm. Note the critical importance of both $\|l_1\|$ and r_{12} in determining the overall beamformer error.

summarised in Figs. 4B and 4C. Fig. 4B shows a single example of the magnetic field vectors measured at an array of 150 sensors; neuromagnetic field from a current dipole in the brain is shown in black. Fields from an external source are in blue. As shown, the vector fields differ dramatically. However, when just taking the radial projection of these field vectors – which are shown in the left-hand maps of Fig. 4C, the two field patterns look similar. Likewise, the field patterns for the polar and azimuthal field projects look similar. However, whilst the radial components are positively correlated, both of the tangential components are negatively correlated. This means that when the radial, polar and azimuthal projections are concatenated, correlation will be reduced compared to use of any one projection alone. Whilst this is only one example, it illustrates the reason why the value of r_{12} is reduced in the triaxial system, compared to the simulated radial systems for external sources of interference. This idea will be addressed further in our discussion.

2.3.3. Interim conclusion

Our analyses show that beamformer error depends on two critical parameters: $\|l_1\|$ (the Frobenius norm of the field measured from the source of interest) and r_{12}, (the similarity between the field patterns for the sources of interest and interference). The former should be maximised whilst the latter minimised. Maximising $\|l_1\|$ is easily achieved by adding sensors; adding tangential measurements (i.e. replacing radial sensors with triaxial sensors) increases $\|l_1\|$ by virtue of effectively tripling the channel count. However, the increase is not as large as that

produced by adding an equivalent number of radial sensors, since on average, the polar and azimuthal fields are smaller than radial fields. However, this theory also suggests that the addition of triaxial sensors has a dramatic effect on r_{12}, for sources of interference outside the brain. We argue that this outweighs the relatively modest effect on $\|l_1\|$, and consequently, particularly in cases where large external interference is expected, a triaxial system will offer a marked advantage over a radial system, even if the latter has a very high channel count. This theory thus provides the basis for the simulations presented in Section 3.

3. Numerical simulation

3.1. Effect of interference on beamformer reconstruction

Based on our analytical insights, we hypothesised that a 150-channel radial system should outperform a 50 sensor triaxial system in the absence of interference (a consequence of the higher forward field norm). However, if interference is introduced (external to the brain), we would expect that the triaxial system would offer improved performance (due to its ability to better separate source topographies (diminish r_{12}). We undertook simulations to test this hypothesis.

3.1.1. Methods

Simulations were based on the systems shown in Fig. 1. For all simulations we employed a spherical volume conductor head model. The simulation comprised three stages:
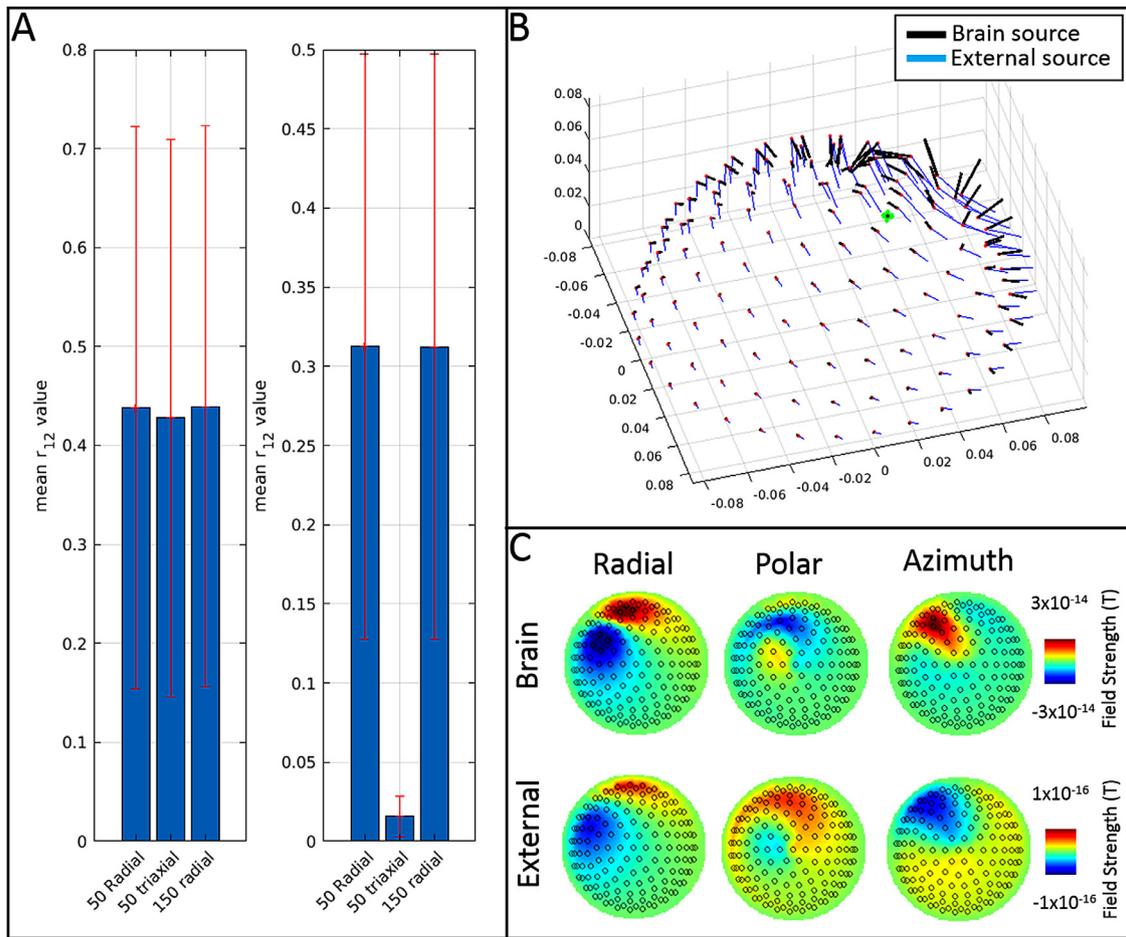
Fig. 4. The effect of array design on r_{12}. A) mean r_{12} values across 25,000 dipole realisations, as a function of array type. Left hand plot shows the case for internal sources; right hand plot shows the case for external sources. B) Example magnetic field vectors for a single internal source of interest (black) and external source of interference (blue). Green dot shows the source of interest C) The same fields decomposed into radial (r), polar (θ) and azimuthal (φ) components and shown as topographical maps. Note the external interference field is smaller due to it's proximity to the head array (we have modelled a current dipole strength of 1 nAm in both cases). Obviously in practice the dipole strength for an external source is larger. (For interpretation of the references to colour in this figure legend, the reader is referred to the web version of this article.)

- **Single Source simulation:** A single source of interest was simulated in the brain. The source was located between 2 cm and 2.4 cm from the surface of the head (sphere) to mimic activity in the cortex. Apart from its depth, the source location was random. Source orientation was tangential to the radial direction, but otherwise random. The source timecourse comprised Gaussian distributed data sampled at 600 Hz, and the root-mean-square amplitude was set to 1 nAm. The forward field was based on a current dipole.
- **Interference generation:** We used two different realisations of interference; external and internal to the brain (i.e. the former representing e.g. laboratory equipment and the latter representing 'brain noise').
  - For **external interference**, we generated 80 sources of magnetic field, at distances ranging from 20 cm to 60 cm from the centre of the head. Source timecourses comprised Gaussian random data and their locations were randomised. All sources were assumed to be current dipoles orientated perpendicular to the vector joining the centre of the head to the dipole location. The source strength was calculated in proportion to the strength of the source of interest. Specifically, assuming $\|l_s\|$ is the forward field norm of the source of interest, $\|l_{int}\|$ is the forward field norm of the interference, and Q_s is the source amplitude, then the interference amplitude was set as $Q_{int} = \alpha Q_s \frac{\|l_s\|}{\|l_{int}\|}$ where α controls the relative strength of interference.

- For *internal interference*, we generated 15 dipoles in the head. These interference sources could take any location, but source orientation was constrained to a tangential plane (defined relative to their location within the sphere). Interference sources were positioned at a minimum of 20 mm, and a maximum of 60 mm from the source of interest (Euclidean distance). Source timecourses were Gaussian random data, and the source amplitudes were set in proportion to the source of interest.
- **Additive noise:** Sensor noise was assumed to be Gaussian random noise, independent, but with equal amplitude, across sensors. This was added with an amplitude of 30 fT.

A total of 300 s of data were simulated in this way. For each iteration of the simulation, different source and interference locations were used and α took values ranging from 0 to 1.4 in steps of 0.1 to increase the impact of interference on the MEG data. (Different source/interference timecourses, and different noise realisations were used for each α.) 25 iterations of the simulation were run. Source and interference timecourses were the same for each system type (50-channel radial, triaxial, and 150-channel radial) although different sensor noise was used for the three systems.

Each dataset, for each system, was processed using a beamformer. Prior to beamforming, we simulated a coregistration error on the sensor locations such that the location and orientation of the sensors used for beamforming were not the same as those used to simulate the data.

Specifically, sensor locations and orientations underwent a 2 mm translational, and 2° rotational affine transformations whose directions were randomised.

Data covariance was calculated in the 0–300 Hz frequency window, and a time-window encompassing the full 300-s simulation. No regularisation was used. To image the source, we adopted a pseudo-Z-statistic approach, which contrasts beamformer projected power to noise. Images were generated within a cube with 12 mm side length, centred on the true source location. The cube was divided into voxels (of isotropic dimension 1 mm) and for each voxel the source orientation was estimated using the direction of maximum signal to noise ratio. A single image was generated per simulation. In each case, the peak pseudo-Z statistic was found and its location used to reconstruct the timecourse of peak activity. We derived three measures of beamformer accuracy.

1. **Localisation accuracy:** We found the location of the peak in the beamformer image and computed its displacement from the true source location. This provided a measure of localisation error.
2. **Timecourse error:** We calculated the sum of squares of the differences between the reconstructed timecourse (at the peak in the beamformer image) and the true timecourse.
3. **Timecourse correlation:** At the location of the peak in the beamformer image we calculated the temporal Pearson correlation between the beamformer-projected source timecourse and the simulated timecourse.

3.1.2. Results

Fig. 5A shows example beamformer images and reconstructed timecourses for the three MEG systems. In the left-hand panel there was no interference ($\alpha = 0$). In the right-hand panel, 80 sources of interference, external to the brain, have been added; each with amplitude equivalent to that of the source of interest ($\alpha = 1$). In both cases the top, centre and bottom panels show the 50-sensor radial, 50-sensor triaxial and 150-sensor radial systems, respectively. As expected with no external interference all three systems faithfully reconstruct the source (the small localisation error likely results from the simulated coregistration error). However, when interference is added, for both radial systems the beamformer image and the source reconstruction are degraded. The triaxial system, in contrast, maintains a faithful representation.

These results are formalised in Figs. 5B, C and D which show timecourse correlation, timecourse error and localisation accuracy, as a function of interference amplitude. As interference is added, both radial systems begin to degrade in performance. In contrast, the triaxial system remains unaffected by the external interference. Note that, with no interference, the 150-channel radial system outperforms the triaxial system as expected. However when interference is introduced, the triaxial gains an advantage.

Fig. 6 shows our summary metrics plotted against interference amplitude for internal sources of interference (i.e. brain noise). Here, the measurement of vector fields with a triaxial system does not help to distinguish between sources and consequently, a triaxial system offers less improvement. Whilst 50 triaxial sensors outperform 50 radial sensors (likely a consequence of the increased lead field norm), 150 radial sensors, in this case, result in a more accurate reconstruction. In fact, further work (not shown) infers that the 50 sensor triaxial device performs approximately equivalently to 80 radial sensors in the presence of internal interference sources. (See also Fig. 2).

3.2. Effect of head movement on beamformer reconstruction

Perhaps the biggest advantage of an OPM system is that the use of lightweight sensors makes it possible for the system to be integrated into a wearable helmet, allowing subjects to move during data acquisition (Boto et al., 2018; Hill et al., 2019). This robustness to motion makes the MEG environment better tolerated by many people. However, in the presence of a background field, motion causes magnetic artefacts since the sensors rotate relative to the background field (or translate in a field gradient). Significant work (Holmes et al., 2018; Iivanainen et al., 2018; Holmes et al., 2019a) has been directed at minimising these background fields/gradients, usually via a combination of advanced passive magnetic screening (i.e. housing the system within a room made from multiple layers of high permeability material) and electromagnetic coils. Using such methods, background fields can be made as low as 1 nT. However, even in these very low field environments, artefacts may still be similar in magnitude to brain activity, and so better ways to supress motion will be important for OPM-MEG to reach its true potential.

In principle, the motion artefact behaves somewhat like external interference, and so given the results in Fig. 5, one might expect a triaxial system to facilitate removal of such artefacts more effectively than a radial system. However, unlike external interference, which typically results in a spatially static field, movement artefact manifests as an apparently moving field. This introduces non-linearly changing field patterns which makes it hard to model. For this reason, we undertook a simulation to assess the performance of our three system types for movement artefact suppression.

3.2.1. Methods

To simulate motion artefacts, we first generated a set of movement parameters. As with any rigid body, we assumed 6 degrees of freedom for the simulated helmet/head – translation in x, y and z, and rotation about x y and z. For each degree of freedom, we simulated a 'motion time series' which collectively would define how the helmet moved relative to a static background field. Motion time series comprised Gaussian random data which were frequency-filtered to the 4 to 8 Hz frequency band (since movement was assumed to be mostly low frequency). Each of the six motion time-series comprised a single common signal (i.e. modelling common movement about multiple axes at the same time) and a separate independent signal (i.e. modelling temporally-independent movements on each axis). The amplitude of the common signal was 5 mm translation and 3° rotation; the amplitude of the independent signal was 2 mm translation and 2° rotation. Following construction of the time series, the motion was applied to the helmet via affine transformation.

We assumed three different conditions for the background field. 1) No field (i.e. so movement will have no effect). 2) A static and uniform background field of $\boldsymbol{B}(\boldsymbol{r}) = [5\ 5\ 5]$ nT (where $\boldsymbol{r}$ represents position) (i.e. rotations will cause artefacts, but translations will have no effect). 3) A static but non-uniform background field. Here $\boldsymbol{B}(\boldsymbol{r}) = \boldsymbol{B}_o + \boldsymbol{G}.\boldsymbol{r}$: $\boldsymbol{B}_o$ (= [5 5 5] nT) is a spatially uniform background field and $\boldsymbol{G}$ is a 3×3 matrix which describes the linear magnetic field gradients with G_{ij} producing the field component $B_{r_i} = G_{ij}r_j$ where $r_{i,j,k} = x, y, z$. We assumed

$$\boldsymbol{G} = \begin{bmatrix} 10 & 5 & 8 \\ 5 & 10 & 5 \\ 8 & 5 & -20 \end{bmatrix} nTm^{-1};$$ note the reflectional symmetry and zero trace of the matrix is imposed by the Maxwell equations. For each time point, the location and orientation of every sensor in the helmet was calculated according to the motion timecourse, and the local field vector calculated. The field 'seen' by the sensor was then estimated as the dot product of the sensitive sensor orientation(s) with the field vector, $\boldsymbol{B}(\boldsymbol{r})$.

OPM sensors come equipped with on-board electromagnetic coils which zero the field at the measurement location; this is a requirement since OPMs must operate close to zero field. This means that, at the start of an experiment (i.e. with the head in its starting position) the fields measured will be zero. At this point, the currents applied to the on-board coils are locked. To simulate this, the artefact was assumed to be the measured field shift between the first timepoint, and all other timepoints. An example of this process is shown in Fig. 7A, for a 150-channel system.

A single dipolar source of 1 nAm-amplitude was simulated at a depth of between 20 mm and 48 mm from the surface of the spherical conductor, with random orientation in the tangential plane. The source was tangentially-orientated and its location randomised. The source time-
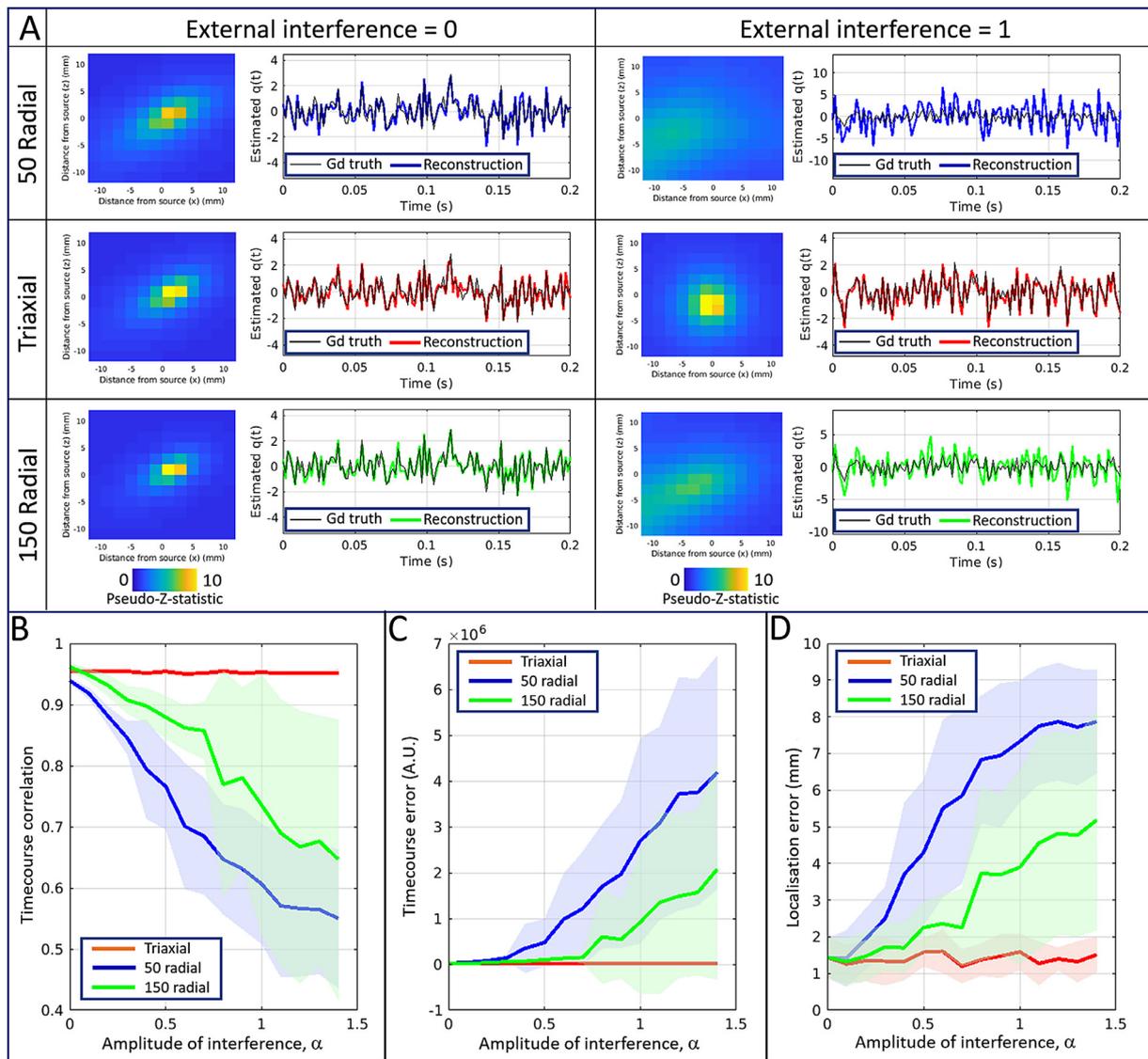
Fig. 5. Beamformer performance with 80 external interference sources. A) Example beamformer images of a simulated source of interest. Line plots show reconstructed timecourses (in nAm) from the peak of the image (coloured lines) overlaid on the true source timecourse (black). Three rows show the three different simulated systems whilst the two columns show results produced with (right) and without (left) interference. B) Correlation between the reconstructed and true source timecourse, as a function of interference amplitude. C) Error on the beamformer timecourse versus interference amplitude. D) Localisation error versus interference amplitude. (For interpretation of the references to colour in this figure legend, the reader is referred to the web version of this article.)

course comprised Gaussian random noise, which was frequency filtered to the 4–8 Hz band to mimic a situation where the source of interest is obfuscated (in terms of frequency) by the movement artefact. Sensor noise corresponding to 15 fT/rHz was also added. This sensor noise was also filtered to the 4–8 Hz band, leading to a standard deviation of 30 fT. For each of the three separate background field conditions, the simulation was run 50 times using a different source of interest on each iteration. To assess the extent to which the beamformer can reconstruct the source we again measured timecourse correlation, timecourse reconstruction error, and localisation error.

3.2.2. Results

In Fig. 7B, our three separate performance metrics are shown in the three rows. The left, centre and right columns show 50-sensor radial, the 50-sensor triaxial, and 150- sensor radial systems, respectively. As in Fig. 5, we see a degradation in performance of the two radial systems as the motion artefact is added, and then made more complex. As would be expected, the 150-channel system performs better than the 50-channel

radial system. However, the triaxial system outperforms both, with little or no loss in performance as the motion artefact is added.

3.2.3. Interim conclusions

The simulations confirmed our theoretical analyses that a triaxial MEG system can offer extremely attractive advantages in terms of interference rejection. In particular, the ability to better distinguish sources of interference (external to the brain) from the neuromagnetic field means that whilst radial arrays are adversely affected by external interference, the triaxial array is much less affected once a beamformer has been applied. In a similar way, if a wearable OPM array is used in which a subject rotates and translates their head in a background field, the effects of the resulting artefact can be better supressed by a triaxial array compared to a radial only array.

4. Experimental verification

The above simulations demonstrate the theoretical advantages of a triaxial MEG system. Obviously experimental verification of
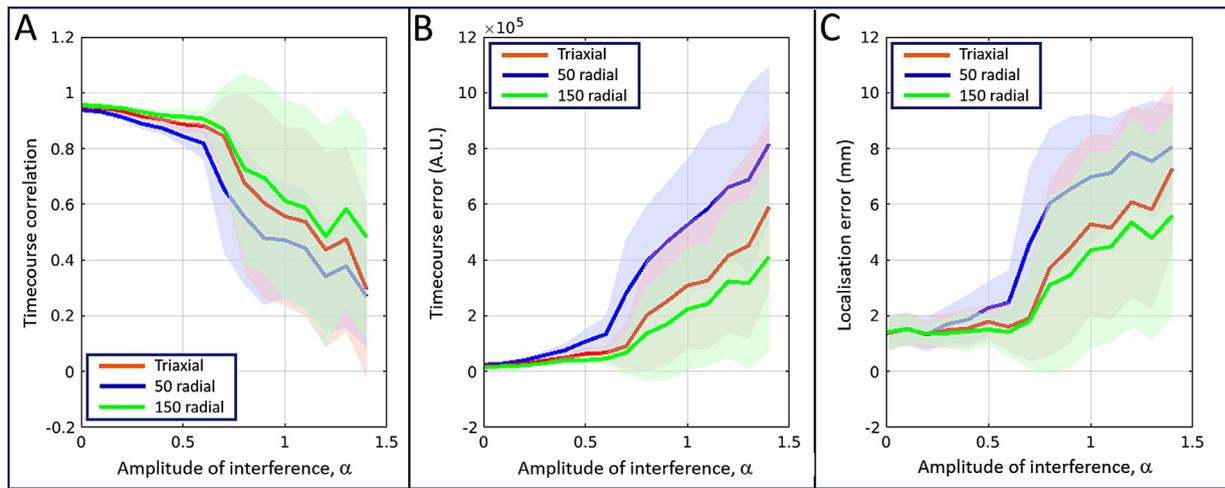
Fig. 6. Beamformer performance with 15 internal interference sources. A) Correlation between the reconstructed and true source timecourse, as a function of interference amplitude. B) Error on the beamformer reconstructed timecourse versus interference amplitude. C) Localisation error versus interference amplitude.

these advantages would be attractive but, whilst triaxial OPMs exist (www.quspin.com), at the time of writing they have not yet been produced in sufficient quantities to support a MEG array. For this reason, we aimed to experimentally verify the triaxial "principle", using a more conventional OPM-MEG array. The fundamental idea behind the triaxial principle is that orienting sensors in different ways helps to differentiate sources of magnetic field inside and outside the brain (by reducing r_{12}). This being the case, we surmised that a similar effect might be achievable by taking a radial-only array and rotating the sensitive axis of a small number of sensors through 90°.

4.1. A system with rotated sensors - simulation

Fig. 8A shows two simulated 50-channel systems; in both cases the sensor locations are identical, however in the system on the right, 5 sensors have had their sensitive axis rotated (sensors circled in black) into the azimuthal orientation. For both systems, we simulated 25 sources of interest in the brain (1 nAm, dipolar, orientated tangentially and location randomised.) For each internal source we simulated 80 sources of external interference (also current dipoles, at a distance between 20 cm and 60 cm from the centre of the head, strengths set as per our previous simulations using the parameter, α). For each pairing of a source of interest and interference source, we measured the correlation between their spatial topographies (i.e. r_{12}) for the radial and 'rotated' systems.

Fig. 8B shows a single example of one source pair. The maps show the topographies of the measured fields from the internal and external sources; notice how the external source topography is altered by the sensor rotation and this leads to a drop in the r_{12} value. Fig. 7C shows all r_{12} values for the radial system, plotted against the equivalent r_{12} values for the system with some rotated sensors. If the rotation of sensors had no effect, then these values would fall along the $y = x$ line (shown in black). However, they consistently fall beneath it (line of best fit shown in blue), implying that r_{12} is, on average, lowered by sensor rotation. Whilst this effect is marginal, we point out that beamformer estimated error is a non-linear function of r_{12}, meaning that even a marginal reduction could yield a relatively large improvement in beamformer performance.

In Fig. 8D, E and F, we have repeated the simulation shown in Fig. 5, using the radial and rotated systems. As expected, even rotating 5 sensors has a relatively large effect, with a significant improvement in performance. Obviously, this effect is not as dramatic as that expected for a complete triaxial system (compare e.g. Fig. 8E with Fig. 5B). Nevertheless this theoretical improvement provides a basis for a simple experiment with an existing 50-channel OPM-MEG array. We hypothesised

that an experimental array with 5 rotated sensors might enable better suppression of interference by a beamformer.

4.2. A system with rotated sensors – experiment

4.2.1. Methods

A single subject (male, aged 25 years, right-handed) took part in the experiment, which was approved by the University of Nottingham Medical School Research Ethics Committee. On each trial of the experiment, the participant was shown a visual stimulus (a picture of a hand) for 2 s; this was followed by 3 s rest. Whilst the stimulus was on the screen, the participant was asked to make continuous abductions of their left index finger. The experiment comprised 50 trials and was repeated 4 times. This paradigm gives a robust response in the beta (13–30 Hz) frequency band.

MEG data were recorded using a 45 channel OPM-MEG array; this array has been described in previous papers (Hill et al., 2020). Sensors were manufactured by QuSpin Inc. and formulated as magnetometers. They were mounted in a 3D printed rigid helmet and their location and orientation with respect to brain anatomy was found using a combination of the known geometry of the 3D printed helmet (which gives sensor locations and orientations relative to the helmet, and each other) and a head digitisation procedure, based upon optical scanning (Hill et al., 2020) (which provides a mapping of the helmet location to the head). Most importantly, in the first and third run of the experiment, sensors were orientated radially (see Fig. 9A, left hand side), while in the second and fourth runs of the experiment, 5 sensors were rotated through 90° (Fig. 9A, right hand side). This gave a similar experimental setup to that simulated in Fig. 8. Note that the axis of rotation was constrained by the 3D printed helmet, and the rotation itself affected simply by changing the sensitive readout axis of the OPM.

4.2.2. Sensor space analysis

Sensor space data were frequency-filtered into the beta band and segmented into trials. For each sensor, and each trial, data were Fourier transformed to provide an amplitude spectrum. We then averaged over all trials, and sensors, in order to visualise how the beta band data were contaminated by artefacts. A source of external interference (caused by nearby laboratory equipment outside the MSR) was found at ~16.7 Hz. The spatial topography (across sensors) of this artefact was measured by taking the magnitude of the amplitude spectrum, at this frequency, across all sensors.
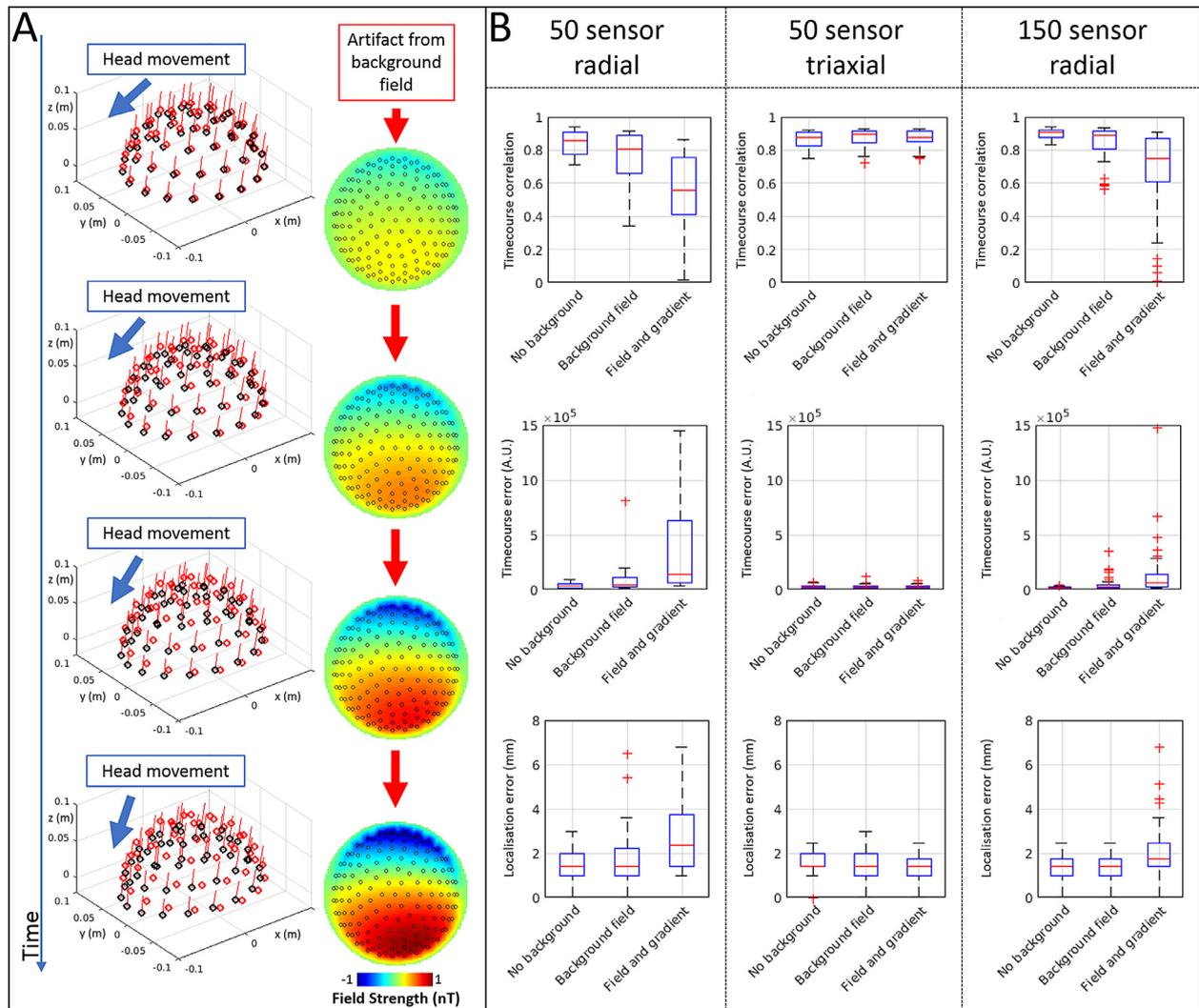
Fig. 7. Motion artefact suppression. A) An example of the simulated motion artefact. In each of the 3D plots, the red circles show the original sensor locations at time zero. The black circles show the sensor locations at 4 consecutive points in time (with time increasing vertically). Note the rotation of the head. The red lines show the direction of the background field at each sensor at each timepoint. The inset field maps show the artefact, which is the change in field between time zero and the current time point. B) Performance of 3 simulated systems in supressing motion artefact. The three columns show the 50-sensor radial, 50-sensor triaxial, and 150-sensor radial systems. The top, centre and bottom rows show timecourse correlation, timecourse error and localisation error respectively. Within each plot we show the associated performance metric for no background field, a uniform field, and a non-uniform field. Notice that performance metrics decline for both radial systems but not for the triaxial device. (For interpretation of the references to colour in this figure legend, the reader is referred to the web version of this article.)

4.2.3. Source space analysis

Data were projected into source space using a beamformer. We computed data covariance in the beta band. Data were segmented into trials and, in order to avoid discontinuities between trials affecting our covariance estimate, a separate covariance matrix was calculated for each trial, and the average over trials used. No regularisation was applied. The forward field was based on a spherical volume conductor model, using the best fitting sphere to the subject's head shape, and the dipole approximation. Data were reconstructed to 78 locations in the cortex, each corresponding to the centroid of a cortical region, defined based on the Automated Anatomical Labelling (AAL) brain atlas. For each AAL region, we computed the data for each trial. Associated amplitude spectra were derived and averaged across trials and regions. This analysis was independently applied to each of the four experimental runs.

To approximate r_{12} in experimental data, for each of the 4 runs, we correlated the source space topography of the interference pattern with the best fitting forward field for each AAL region. This was done independently for each run and we plotted averaged values from runs 1 and 3, against averaged values from runs 2 and 4.

Finally, we included a conventional analysis whereby, at each AAL region, we contrasted oscillatory amplitude in an active window (1–2 s) to oscillatory amplitude in a control window (3–4 s). This was normalised by the value for the control window to estimate fractional change in beta amplitude induced by the task. We also plotted the trial-averaged beta amplitude for an AAL region in right motor cortex.

4.2.4. Results

Fig. 9B shows the sensor-space data. The line plot shows Fourier-derived amplitude spectra averaged over channels, with a clear artefact at ~16.7 Hz. Data from runs 1 and 3 (radial sensors) are shown in black and blue; runs 2 and 4 data (radial and tangential sensors) are shown in red and green. Note that the artefact is consistent across all four runs. The spatial topography of the artefact is shown inset.

The equivalent amplitude spectra for the source-space-projected data are shown in Fig. 9C. In all four cases, the 16.7 Hz artefact has been reduced in relative amplitude compared to channel-space data, however this reduction is more pronounced in the data recorded with the five rotated sensors. The distribution of this improvement
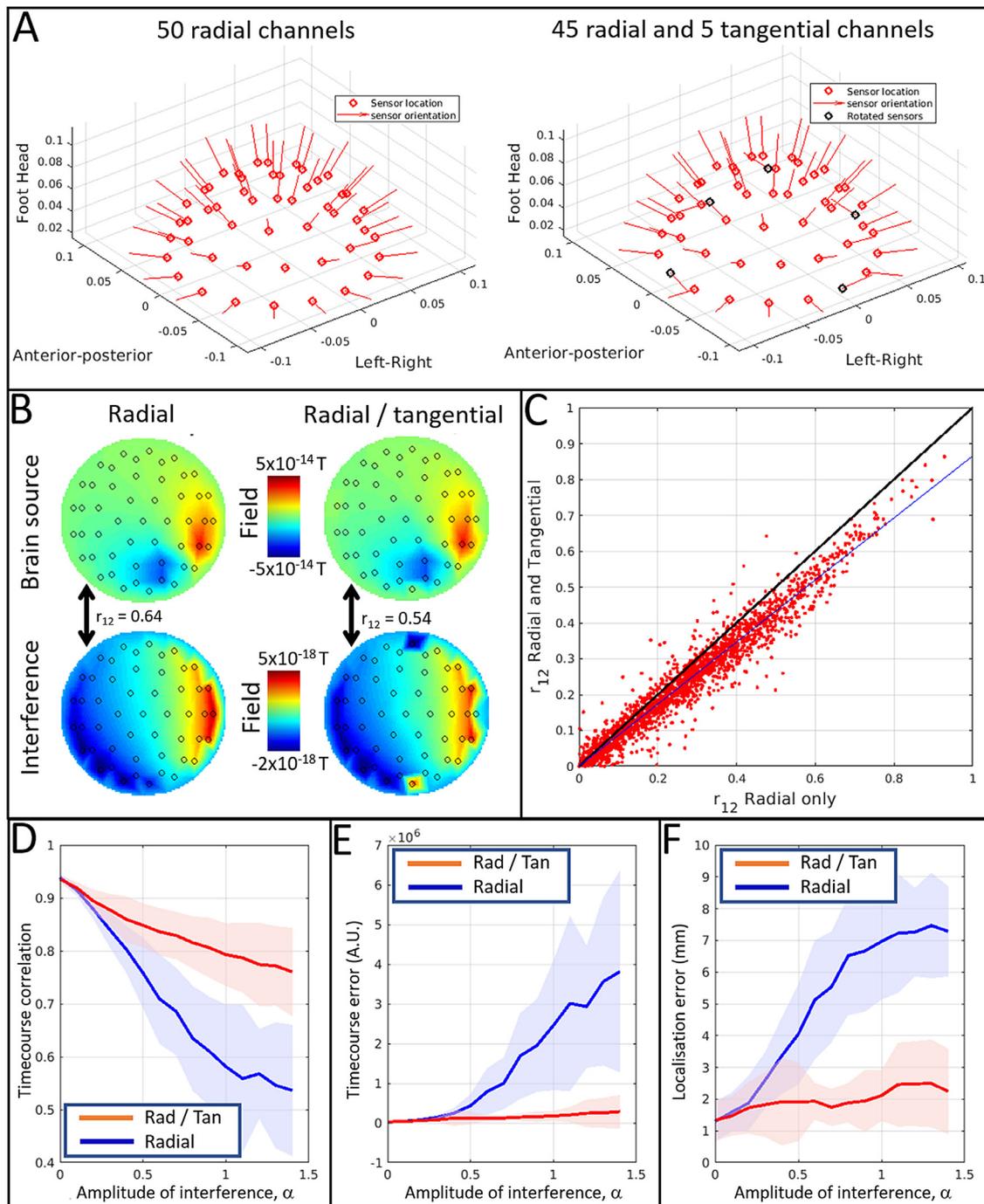
Fig. 8. the effect of sensor rotation – simulation: A) two simulated OPM MEG arrays. Both have 50 channels with sensors in identical locations. However, the system on the left has all channels orientated radially, whereas the system on the right has 45 radial and 5 tangential sensors (rotated sensors circled in black). B) Example simulated field patterns for a source internal to the brain (upper row) and external to the brain (lower row) measured using the radial (left) and rotated (right) systems. Note that the smaller scale of the external source is due to it's proximity to the array; i.e. we maintain the dipole amplitude at 1 nAm for both brain and interference sources, the interference amplitude is then set by the parameter, α. C) r_{12} values for the radial system (x-axis) versus rotated system (y axis). Each point (red) represents a different internal/external source pair. Black line shows $y = x$. blue line shows line of best fit to the data. D) Timecourse correlation versus amplitude of external interference. E) Timecourse reconstruction error versus amplitude of external interference. F) Localisation error versus amplitude of external interference. In D, E and F the blue line shows the radial system and the red line shows the system with 5 rotated sensors. (For interpretation of the references to colour in this figure legend, the reader is referred to the web version of this article.)

across the brain is shown in the inset image (calculated as a relative change). This provides experimental evidence that the primary findings of the theory and simulations presented above can be realised. Estimated r_{12} are shown in Fig. 9D; note that, on average, the forward fields from the AAL regions are more similar to the spatial to-

pography of the artefact for the radial system compared to the rotated system.

Finally, for completeness Fig. 9E shows the beta modulation produced by the task: blue indicates a loss of beta power during the time window where the subject was making controlled left index finger move-
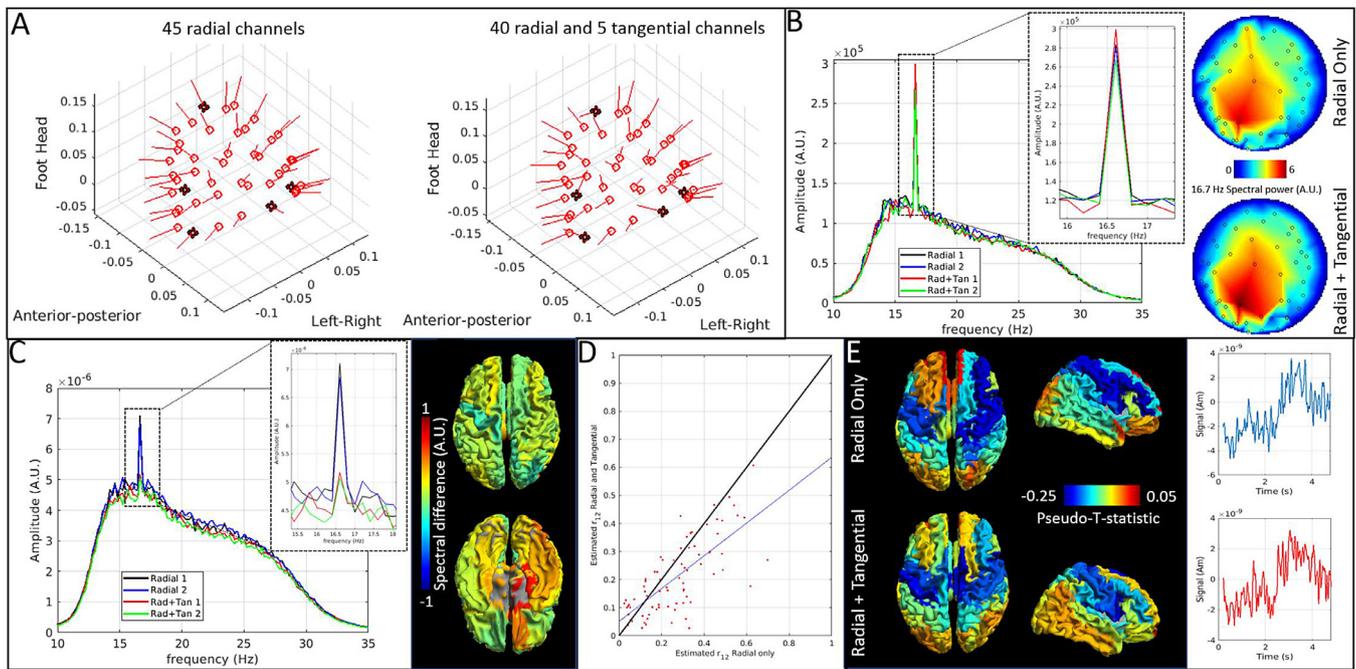
Fig. 9. *Experimental results: A) Two experimental OPM arrays. The left-hand array has only radial sensors; the right-hand array has 40 radial and 5 tangential sensors. B) Trial- and sensor-averaged Fourier amplitude spectra showing the beta-band-filtered data with an artefact due to external interference at 16.7 Hz. Spatial topography of the interference peak is shown on the right-hand side. C) Trial- and region-averaged Fourier amplitude spectra in source space, showing the beta band filtered data with an artefact due to external interference at 16.7 Hz. Note the clear difference in 16.7-Hz artefact between the radial and rotated sensor layouts. Cortical distribution of improvement afforded by sensor rotations are shown on the right. The spectral difference is calculated as the difference in mean amplitude of the 16.7 Hz peak for the radial and rotated systems, divided by the sum of the same quantities D) An approximation of correlation between internal sources (lead fields) and interference topography. Red markers show 78 regions with r_{12} for the radial system plotted on the x axis, and r_{12} for the rotated system on the y axis. E) Task-induced beta modulation across 78 AAL regions. Blue indicates a decrease in oscillatory power during movement compared to rest. Inset timecourses show trial averaged beta amplitude envelope in right motor cortex. (For interpretation of the references to colour in this figure legend, the reader is referred to the web version of this article.)*

ments. Note that the main effects are well localised to sensorimotor cortices. Both the radial, and rotated systems offer reasonable localisation. The inset line plots show beta modulation in right motor cortex, averaged over trials, with the expected loss in beta power during movement (the movement-related beta decrease – MRBD) and an increase (above baseline) immediately following movement cessation (the post-movement beta rebound – PMBR) clearly delineated.

5. Discussion

A number of recent studies have shown that OPMs offer a potential step change for MEG technology, however one area that has not been well documented is that the flexibility of placement of OPMs, coupled with new designs of sensor, might offer array designs which can aid magnetic source imaging. Cryogenic sensors rely on pick up coils which can be bulky, and whilst vector field measurements have been made successfully using SQUID technology (Haueisen et al., 2012; Nurminen et al., 2013), the physical limitations of coils makes it difficult to measure 3 field orientations at the same location, and triaxial SQUID systems have not reached mainstream use. In contrast, OPM design can facilitate co-localised, vector-field measurements at relatively little extra cost or complexity (Borna et al., 2020), making a multi-channel whole-head triaxial system possible. Even with single axis OPMs, their miniaturised design and the flexibility to easily change the orientation of the sensitive axis offers a means to alter MEG arrays in a way that can offer improved performance. In this paper, our aim was to demonstrate how this flexibility can be exploited.

Our analytical models provided insights into how a MEG array should be optimised to maximise the benefits of spatial filtering. Our single-source model showed that a key parameter is $\|l\|$ – the norm of the forward field of the source of interest. This can be thought of as the total amount of signal picked up across the array from an active source. We showed that the total error in a beamformer reconstruction goes as $1/\|l\|$, meaning that as $\|l\|$ increases, the error will be diminished. The easiest means to increase $\|l\|$ is via the addition of extra sensors to an array and so, by effectively tripling the channel count, a triaxial system immediately adds value. However, we also showed, in agreement with previous work (Iivanainen et al., 2017), that there is an advantage to radially orienting the sensitive axes of the additional sensors, since radial fields are larger than the tangential fields. This led to the finding that a triaxial system with 50 sensors has an approximately equivalent performance to a radial system with 80 sensors, *in the absence of interference*.

Analytical analyses using two sources showed that the second key parameter to consider when designing a MEG array is r_{12} – the forward field correlation between the two sources. This tells us that if a source of interference has a similar sensor space topography to the source of interest, then this will lead to a large error in reconstruction. However, using a beamformer, the total error on a reconstruction is a non-linear function of r_{12} meaning that even a modest improvement (reduction) in r_{12} can yield a relatively large drop in error. (This is in contrast to other source localisation algorithms, such as dipole fitting, where reconstruction error would be a linear function of r_{12} – this in itself shows the advantage of the beamformer's adaptive nature.) This non-linearity means that even a relatively small manipulation of the array lay-out can result in a small reduction in r_{12}, and large improvement in reconstruction accuracy. Further analysis showed that the introduction of triaxial sensors can have a large effect on r_{12}, and consequently the addition of triaxial sensors, or even rotation of a few unidirectional sensors, enables better interference rejection.

The means by which array manipulation affects r_{12} is shown by the simple cartoon in Fig. 10. Here we show a very simple three sensor array. In the upper schematic we see a field (blue arrows) generated
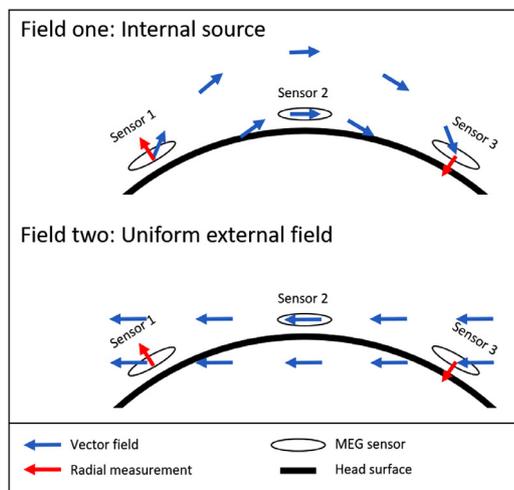
Fig. 10. Schematic showing how two very different fields can appear similar when measured by radially orientated sensors. Upper plot shows a field originating from a source in the brain. Lower plot shows a uniform field originating outside the brain. In both cases the blue arrows show the field orientation; red arrows show the effective field picked up by a radially orientated sensor. (For interpretation of the references to colour in this figure legend, the reader is referred to the web version of this article.)

by the brain. Assuming radially orientated sensors then sensor 1 would measure a field directed out of the head (a positive field – red arrow); sensor 3 would detect a field directed into the head (a negative field – red arrow); sensor 2 would pick up nothing. In the lower schematic we see a very different uniform field generated by an external source. However, because of the orientation of the radial sensors, again sensor 1 measures a positive field, sensor 3 a negative field, and sensor 2 nothing. This means, despite very different fields, the measured topography would be highly correlated. In contrast, if we simply rotated the sensitive axis of sensor two so that it measures tangentially, it's easy to see that the measurements made would show that the two fields are in opposite directions. This would cause a reduction in the correlation. This is the basic premise of the effects shown throughout this paper.

The analytical insights enabled formulations of hypotheses regarding beamformer behaviour, which have been tested in simulations. Fig. 5 shows that the introduction of triaxial measurements has a marked effect on the ability of a beamformer to cancel external sources of interference – such sources could be caused by nearby laboratory equipment, or even sources of magnetic field in the body such as the heart or skeletal muscles. In conventional MEG systems, two techniques to remove external interference have become common, either software approaches (Taulu and Simola, 2006) (see also below) or reference arrays (Vrba and Robinson, 2001). In the latter case, one typically constructs a separate array of magnetometers that are far enough from the sensors to be (mostly) insensitive to the neuromagnetic field, but close enough to measure similar interference. Such arrays are extremely successful in reducing background interference and are commonplace in many cryogenic systems. Similar strategies have also been used for OPM measurements (Boto et al., 2017). However, building a reference array on a wearable helmet is a challenge since one needs sensors displaced from the scalp surface which would likely make the helmet design impractical. Nevertheless the need for interference rejection is critical, particularly given that most OPMs are formed as magnetometers which are more susceptible to external interference than the more commonly employed gradiometers in cryogenic systems. The fact that a triaxial system offers a marked improvement in noise characteristics is therefore important; it potentially allows a means to eliminate the need for bulky and costly reference arrays.

In addition to an enhanced ability to supress external interference, our results suggest that the triaxial array is similarly advantageous when cancelling the effect of subject head movement in a background magnetic field. This finding is also likely to be important: one of the major advantages of OPM-MEG over conventional MEG is that the system can be fabricated inside a wearable helmet enabling head movement during a scan. However, in the presence of a background field, such movement tends to generate interference – particularly at low frequency. A triaxial system enables better differentiation of the neuromagnetic field from the interference generated by movement, and a beamformer exploits this to supress the motion artefact in a way that it cannot when considering only radial field measurements. This again suggests that a triaxial array design could be extremely advantageous for wearable OPM based technology, where subjects can move.

At the time of writing, whilst the viability of triaxial OPMs has been demonstrated, these sensors do not yet exist in sufficient quantities to fabricate a complete working MEG array. For this reason, our practical demonstration was limited to rotating a small number of sensors in a standard OPM array. Simulations showed that even this relatively small change should yield a measurable reduction in error on a beamformer reconstructed source, and our experimental verification showed that, as predicted, the amplitude of a known interference peak was reduced. This simple demonstration provides confidence that the findings of our analytical work can be realised experimentally.

There are a number of limitations of the current study. First, everything above is considered for the case in which source reconstruction is undertaken using a beamformer spatial filter. Beamforming is popular, but it is by no means the only method to process MEG data and it remains to be seen whether similar advantages could be realised for other algorithms. However, a brief analysis of the mathematics of dipole fitting suggests that r_{12} is again a critical parameter. It would be extremely unlikely that the reduction in r_{12} afforded by the triaxial array does not lead to advantages for other approaches to source localisation. In addition, previous work (Nurminen et al., 2013) has shown that tangential field measurements markedly improves the performance of signal space separation (a commonly used interference rejection algorithm). Specifically, Nurminen et al. showed that the addition of 18 tangentially orientated sensor elements (each containing a magnetometer and 2 gradiometers) to a 306 channel cryogenic MEG system afforded a 100% increase in software enabled interference reduction. It is therefore highly likely that both source localisation methods, and interference rejection algorithms, would benefit from triaxial measurement.

A second limitation relates to the choice of forward field model. Here, we used a simple spherical volume conductor forward model which served as a useful approximation; it enabled an appreciation of the scalp level topography of the magnetic field vectors generated by neural current, and how these spatial patterns differ from those generated by external interference sources. For both radial and tangentially orientated sensors, the field patterns produced by this simple model are visually similar to those measured experimentally (Haueisen et al., 2012; Borna et al., 2017) and (most importantly) the critical property – that the addition of tangential field measurements helps differentiate neural sources from external interference – is unlikely to change even if alternative forward models were used. However, in experimental practice the single sphere model will lead to errors when modelling fields from a real brain. This is particularly the case for tangentially orientated fields, which are more affected by volume currents than the radial field. Indeed, for the simple sphere model, if only the radial component of field is considered then the volume current term tends to zero (Sarvas, 1987). If tangential fields are measured, volume currents do contribute; they are implicitly incorporated into the expression for total field (Sarvas, 1987) but are independent of conductivity using the simple spherical model (Sarvas, 1987; Van Uitert et al., 2003). However, for realistic head shapes, volume currents do become dependant on conductivity and the importance of modelling this is now well established (Van Uitert et al., 2003; Stenroos et al., 2014; Iivanainen et al.,

2017). Indeed, taking into account the difficulty in modelling volume currents alongside the lower overall field amplitude, Iivanainen et al. (Iivanainen et al., 2017) argue that radial measurements remain the optimal choice for MEG. However, the attractive interference rejection properties demonstrated here suggest that triaxial measurement is likely advantageous. But to realise this advantage, in future experimental implementations it will be critical to use advanced forward field solutions. With realistic forward models (e.g. BEM) readily available in most open source toolboxes, this is unlikely to prove a significant barrier.

Finally, a significant practical limitation relates to the fact that OPMs are subject to errors caused by crosstalk; that is, the measurement at one sensor is affected by the presence of nearby sensors. This is true for all sensor arrays but is likely to be particularly problematic for triaxial sensors due to the orientation of modulation fields. Specifically, the presence of other sensors in close proximity causes changes to both the gain and sensitive access of an OPM. If not controlled, these errors would likely render MEG forward modelling inaccurate, and consequently the efficacy of source localisation algorithms like beamforming would be reduced dramatically. It is therefore likely that exploitation of a complete triaxial array, in the way described in this paper, would require a solution to the crosstalk problem. However, this again is not an insurmountable barrier; the physics of crosstalk within an OPM array should be relatively straightforward to characterise, and so this is unlikely to prove fatal to triaxial MEG design.

Conclusion

An untapped advantage of OPM-MEG is that OPMs enable the simultaneous co-localised measurement of field components along multiple axes, and thus characterisation of the magnetic field vector. Here, we have shown that this extra information can significantly improve images or timecourses of electrical activity, reconstructed using an adaptive beamformer. Using simulations, we have demonstrated that the effect of an optimised array on our ability to differentiate real brain activity from sources of magnetic interference (external to the brain) is dramatic. Further, a triaxial system has been shown to offer a marked improvement on elimination of artefact caused by head movement in ambient magnetic fields. Theoretical results have been supplemented by a real experimental recording demonstrating improved interference reduction during a motor task. These findings offer new insights into how future OPM-MEG instrumentation can be designed with vastly improved performance.

Author contributions

- **Matthew Brookes:** Conceptualization; Data curation; Formal analysis; Funding acquisition; Investigation; Methodology; Project administration; Software; Validation; Visualization; Writing - original draft; Writing - review & editing
- **Elena Boto:** Conceptualization; Data curation; Formal analysis; Investigation; Methodology; Project administration; Software; Validation; Visualization; Writing - review & editing
- **Molly Rea:** Methodology; Software; Validation; Visualization; Writing - review & editing
- **Vishal Shah:** Conceptualization; Methodology; Writing - review & editing
- **James Osborne:** Conceptualization; Methodology; Writing - review & editing
- **Niall Holmes:** Conceptualization; Methodology; Software; Writing - review & editing
- **Ryan Hill:** Conceptualization; Methodology; Software; Writing - review & editing
- **James Leggett:** Project administration; Writing - review & editing
- **Natalie Rhodes:** Visualization; Writing - original draft; Writing - review & editing
- **Richard Bowtell:** Conceptualization; Funding acquisition; Methodology; Writing - review & editing

Data availability

All data available on request

Acknowledgements

APPENDIX A: Analytical analysis of a single source with Gaussian sensor noise

Here, we aim to derive an expression for the accuracy of a beamformer reconstruction of a single dipolar source in the brain with Gaussian noise at the MEG sensors. We assume that the location and orientation, θ, chosen for the beamformer coincides with the true location and orientation of the source. We also assume an accurate forward model, meaning that $l_\theta \rightarrow l$. Via substitution of Eq. (4) into Eq. (1), we get

$$\hat{q}(t) = \boldsymbol{w}^T \boldsymbol{l}q(t) + \boldsymbol{w}^T \boldsymbol{e}(t). \tag{A1}$$

Here, $\hat{q}(t)$ represents the beamformer estimated reconstruction of the true source timecourse $q(t)$, and $\boldsymbol{w}$ is the N-dimensional vector of beamformer weights tuned to the true source location and orientation. $\boldsymbol{e}(t)$ represents sensor error. By definition (see Eq. (2)) $\boldsymbol{w}^T \boldsymbol{l} = 1$, and so

$$\hat{q}(t) = q(t) + \boldsymbol{w}^T \boldsymbol{e}(t) \tag{A2}$$

and inserting Eq. (3) we find that

$$\hat{q}(t) = q(t) + \frac{\boldsymbol{L}^T \boldsymbol{C}^{-1} \boldsymbol{e}(t)}{\boldsymbol{L}^T \boldsymbol{C}^{-1} \boldsymbol{L}} \tag{A3}$$

Eq. (A3) shows that the beamformer-estimate is a true reflection of the real source timecourse, $q(t)$, but with additive noise projected through the beamformer weights.

We now consider the analytical form of the data covariance, $\boldsymbol{C}$ and its inverse $\boldsymbol{C}^{-1}$. For the simple case of a single source, if we assume that the source timecourse is temporally uncorrelated with the sensor noise, we can write

$$\boldsymbol{C} = E(\boldsymbol{bb}^T) = E((\boldsymbol{l}q(t) + \boldsymbol{e}(t))(\boldsymbol{l}q(t) + \boldsymbol{e}(t))^T) \approx Q^2 \boldsymbol{ll}^T + v^2 \boldsymbol{I} \tag{A4}$$

where Q represents the standard deviation of $q(t)$. Using the Sherman-Morrison-Woodbury matrix inversion lemma, we can show that

$$\boldsymbol{C}^{-1} = \frac{1}{v^2} \left(\boldsymbol{I} - f \frac{\boldsymbol{ll}^T}{\|\boldsymbol{l}\|^2} \right) \tag{A5}$$

where

$$f = \frac{Q^2 \|\boldsymbol{l}\|^2}{v^2 + Q^2 \|\boldsymbol{l}\|^2} \tag{A6}$$

is a measure of the effective signal to noise ratio of the source, and scales between 0 and 1. The quantity $\|\boldsymbol{l}\| = \sqrt{\boldsymbol{l}^T \boldsymbol{l}}$ is the Frobenius norm of the forward field vector.

We now let $P = \boldsymbol{w}^T \boldsymbol{C}\boldsymbol{w} = \frac{1}{\boldsymbol{l}^T \boldsymbol{C}^{-1} \boldsymbol{l}}$ and we substitute Eq. (A5) into Eq. (A3), thus,

$$\hat{q}(t) = q(t) + P\boldsymbol{l}^T \left(\frac{1}{v^2} \left(\boldsymbol{I} - f \frac{\boldsymbol{ll}^T}{\|\boldsymbol{l}\|^2} \right) \right) \boldsymbol{e}(t) = q(t) + \frac{P}{v^2} \left(\boldsymbol{l}^T \boldsymbol{e}(t) - f \frac{\boldsymbol{l}^T \boldsymbol{ll}^T \boldsymbol{e}(t)}{\|\boldsymbol{l}\|^2} \right). \tag{A7}$$

Recognising that $\|\boldsymbol{l}\|^2 = \boldsymbol{l}^T \boldsymbol{l}$ and simplifying we see that

$$\hat{q}(t) = q(t) + \frac{P}{v^2} \boldsymbol{l}^T \boldsymbol{e}(t)(1 - f) \tag{A8}$$

We now also recognise that P depends on the data covariance and so

$$P^{-1} = l^T C^{-1} l = l^T \left(\frac{1}{v^2} \left(I - f \frac{ll^T}{\|l\|^2} \right) \right) l = \frac{1}{v^2} \left(l^T l - f \frac{l^T ll^T l}{\|l\|^2} \right)$$
$$= \frac{\|l\|^2}{v^2} (1 - f) \tag{A9}$$

So combining Eqs. (A8) and A9 we see that our beamformer estimated timecourse becomes

$$\hat{q}(t) = q(t) + \frac{1}{\|l\|^2} l^T e(t). \tag{A10}$$

To simplify matters further, we can also write that the vector $e(t)$, which represents the sensor noise across the N sensors can be written as $v\varepsilon(t)$, where v is the standard deviation of the sensor noise and we model ε as a Gaussian random process with unit standard deviation. The final expression for $\hat{q}(t)$ then becomes,

$$\hat{q}(t) = q(t) + \frac{v}{\|L\|^2} l^T \varepsilon(t). \tag{A11}$$

This equation relates only to a single timepoint, and to compute error over all time, E_{tot}, we calculate the square root of the sum of squared differences between the reconstructed and the true timecourse as per Eq. (6). Combining Eq. (A1)1 and Eq. (6) we get

$$E_{tot} = \frac{v}{\sqrt{M} \|l\|^2} \sqrt{\sum_{i=1}^{M} \left(l^T \varepsilon_i \right)^2} = \frac{v}{\sqrt{M} \|l\|^2} \sqrt{\sum_{i=1}^{M} \left(\sum_{j=1}^{N} l_j \varepsilon_{ij} \right)^2} \tag{A12}$$

where M is the number of time points and N is the number of MEG channels. Fortunately, the term $(\sum_{j=1}^{N} l_j \varepsilon_{ij})^2$ is simplified considerably because ε_{ij} is a random process. This means that the cross terms in the square will likely sum to close to zero and can be ignored. Also, noting that $E(\varepsilon_{ij}^2) = 1$, this means that

$$E_{tot} = \frac{v}{\|l\|}. \tag{A13}$$

In other words, the total error in our beamformer reconstruction, for a single source with random noise, scales linearly with noise amplitude (as one might expect) and is inversely proportional to the Frobenius norm of the forward field from the source.

APPENDIX B: Analytical analysis of 2 sources with Gaussian noise

Whilst the analysis in Appendix A is instructive, it is not realistic to expect only a single source to be 'active' in MEG data. It is therefore helpful to extend our analytical treatment to the case of two sources with Gaussian sensor noise. As shown in the main text, in this case the beamformer reconstruction is given by

$$\hat{q_1} = q_1 + w_1^T l_2 q_2 + w_1^T e = q_1 + \delta q_2 + \varepsilon. \tag{B1}$$

Note the two error terms. The first ($\delta q_2 = w_1^T l_2 q_2$) is interference generated by the second source, and the second ($\varepsilon = w_1^T e$) is due to projected sensor noise. We now deal with these two error terms separately.

Error from source 2

The magnitude of interference from source 2 is modulated by $\delta = w_1^T l_2$. Substituting for the beamformer weights we can write that

$$\delta = \frac{l_1^T C^{-1} l}{l_1^T C^{-1} l_1} = P_1 l_1^T C^{-1} l_2 \tag{B2}$$

Where $P_1 = \frac{1}{l_1^T C^{-1} l_1}$ is the projected total power at the location/orientation of the source. To find an expression for δ, we need an analytical form of both the covariance matrix and its inverse in the case of two sources with Gaussian noise. Assuming no temporal correlation

between either of the two source timecourses, or the sensor noise, then

$$C = q_1^2 l_1 l_1^T + q_2^2 l_2 l_2^T + v^2 I \tag{B3}$$

and by the matrix inversion lemma,

$$C^{-1} = \frac{1}{v^2} \left[I - \frac{1}{1 - f_1 f_2 \cos^2(\lambda_{12})} \left\{ f_1 \frac{l_1 l_1^T}{\|l_1\|^2} + f_2 \frac{l_2 l_2^T}{\|l_2\|^2} \right. \right.$$
$$\left. \left. - f_1 f_2 \cos(\lambda_{12}) \frac{l_2 l_1^T + l_1 l_2^T}{\|l_1\| \|l_2\|} \right\} \right]. \tag{B4}$$

As before, f_1 and f_2 represent ratio of signal to sensor noise for the two sources (see Eq. (13)). The quantity

$$\cos(\lambda_{12}) = \frac{l_1^T l_2}{\|l_1\| \|l_2\|} = r_{12} \tag{B5}$$

is reflective of the similarity of the forward fields for sources 1 and 2; it is mathematically related to Pearson correlation. Substituting Eq. (B4) into Eq. (B2) we find that

$$\delta = \frac{P_1}{v^2} \left[l_1^T l_2 - \frac{1}{1 - f_1 f_2 r_{12}^2} \left\{ f_1 \frac{l_1^T l_1 l_1^T l_2}{\|l_1\|^2} + f_2 \frac{l_1^T l_2 l_2^T l_2}{\|l_2\|^2} \right. \right.$$
$$\left. \left. - f_1 f_2 r_{12} \frac{l_1^T l_2 l_1^T l_2 + l_1^T l_1 l_2^T l_2}{\|l_1\| \|l_2\|} \right\} \right] \tag{B6}$$

Which simplifies to

$$\delta = \frac{P_1 \|l_1\| \|l_2\|}{v^2} \left[\frac{r_{12}(1 - (f_1 + f_2) + f_1 f_2)}{1 - f_1 f_2 r_{12}^2} \right] \tag{B7}$$

Noting that

$$P_1^{-1} = \frac{1}{v^2} \left[l_1^T l_1 - \frac{1}{1 - f_1 f_2 r_{12}^2} \left\{ f_1 \frac{l_1^T l_1 l_1^T l_1}{\|l\|_1^2} + f_2 \frac{l_1^T l_2 l_2^T l_1}{\|l\|_2^2} \right. \right.$$
$$\left. \left. - f_1 f_2 \, r_{12} \frac{l_1^T l_2 l_1^T l_1 + l_1^T l_1 l_2^T l_1}{\|l\|_1 \|l\|_2} \right\} \right] \tag{B8}$$

which simplifies to

$$P_1^{-1} = \frac{\|l_1\|^2}{v^2} \left[\frac{1 - f_1 + (f_1 f_2 - f_2) r_{12}^2}{(1 - f_1 f_2 r_{12}^2)} \right] \tag{B9}$$

We can now substitute for P_1 in Eq. (B7) giving

$$\delta = \frac{\|l_2\|}{\|l_1\|} r_{12} \left[\frac{1 - (f_1 + f_2) + f_1 f_2}{1 - f_1 + (f_1 f_2 - f_2) r_{12}^2} \right] \tag{B10}$$

Which simplifies to

$$\delta = \frac{\|l_2\|}{\|l_1\|} r_{12} \left[\frac{1 - f_2}{1 - f_2 r_{12}^2} \right] \tag{B11}$$

This expression therefore shows that the extent of interference from source two is critically dependant on r_{12}.

Error from sensor noise

ε, represents the noise from the MEG sensors projected through the beamformer weights. This is analogous to the sensor noise in the single dipole case (second term in Eq. (A1)1), but is complicated because the beamformer weights are now based on data from 2 sources. Mathematically, ε is given by

$$\varepsilon = P L_1^T C^{-1} e, \tag{B12}$$

and substituting for C^{-1} we get

$$\varepsilon = \frac{P_1}{v^2}\left[l_1^T e - \frac{1}{1 - f_1 f_2 r_{12}^2}\left\{f_1 \frac{l_1^T l_1 l_1^T e}{\|l_1\|^2} + f_2 \frac{l_1^T l_2 l_2^T e}{\|l_2\|^2} \right.\right.$$
$$\left.\left. - f_1 f_2 r_{12} \frac{l_1^T l_2 l_1^T e + l_1^T l_1 l_2^T e}{\|l_1\|\|l_2\|}\right\}\right], \tag{B13}$$

which can be written as

$$\varepsilon = \frac{P_1 \|l_1\|\sqrt{N}}{v}\left[r_{1e} - \frac{1}{1 - f_1 f_2 r_{12}^2}\left\{f_1 r_{1e}(1 - f_2 r_{12}^2) + f_2 r_{12} r_{2e}(1 - f_1)\right\}\right] \tag{B14}$$

Here $r_{1e} = \frac{l_1^T e}{\|l_1\|\|e\|}$ represents the sensor space correlation between the spatial topography of source 1, and the vector representing sensor error. Likewise $r_{2e} = \frac{l_2^T e}{\|l_2\|\|e\|}$ represents the sensor space correlation between the spatial topography of source 2, and the sensor error. Now substituting for P_1 gives

$$\varepsilon = \frac{v\sqrt{N}}{\|l_1\|}\left[r_{1e}\left(1 - \frac{f_1 - f_1 f_2 r_{12}^2}{1 - f_1 f_2 r_{12}^2}\right) - r_{2e}\frac{(f_2 r_{12} - f_1 f_2 r_{12})}{1 - f_1 f_2 r_{12}^2}\right]$$
$$\left[\frac{1 - f_1 f_2 r_{12}^2}{1 - f_1 + (f_1 f_2 - f_2)r_{12}^2}\right] \tag{B15}$$

Which simplifies to give

$$\varepsilon = \frac{v\sqrt{N}}{\|l_1\|}\left[r_{1e}\left(\frac{1}{1 - f_2 r_{12}^2}\right) - r_{2e}\left(\frac{f_2 r_{12}}{1 - f_2 r_{12}^2}\right)\right] \tag{B16}$$

Error over all time

Unfortunately, Eq. (B1)6 only relates to a single timepoint (i.e. r_{1e} and r_{2e} change on each noise realisation, and q_2 is a function of time. For this reason, it is useful to consider the total error across all timepoints. Substituting Eq. (B1) into Eq. (15) we find that

$$E_{Tot}^2 = \frac{1}{M}\sum_{i=1}^{M}(\delta q_{2i} + \epsilon_i)^2, \tag{B17}$$

where i indexes time. Assuming that q_{2i} and ϵ_i are temporally uncorrelated, we can write the total error as two independent terms, thus

$$E_{Tot}^2 = \frac{1}{M}\sum_{i=1}^{M}\left[(\delta q_{2i})^2 + (\epsilon_i)^2\right]. \tag{B18}$$

Noting that $E(q_{2i})^2 = Q_2^2$, the total error due to interference from the second source is given by

$$E_{source}^2 = \frac{1}{M}\sum_{i=1}^{M}(\delta q_{2i})^2 = \delta^2 Q_2^2 = \frac{Q_2^2\|l_2\|^2}{\|l_1\|^2}r_{12}^2\left[\frac{1 - f_2}{1 - f_2 r_{12}^2}\right]^2. \tag{B19}$$

Error due to sensor noise is somewhat more complex to deal with, but from Eq. (B1) we can write that

$$E_{noise}^2 = \frac{1}{M}\sum_{i=1}^{M}(\epsilon_i)^2 = \frac{1}{M}\sum_{i=1}^{M}\frac{v^2 N}{\|l_1\|^2}(ar_{1e} - br_{2e})^2 \tag{B20}$$

where $a = (\frac{1}{1 - f_2 r_{12}^2})$ and $b = (\frac{f_2 r_{12}}{1 - f_2 r_{12}^2}) = f_2 r_{12} a$. Expanding the square this becomes

$$E_{noise}^2 = \frac{1}{M}\sum_{i=1}^{M}\frac{v^2 N}{\|l_1\|^2}(a^2 r_{1e}^2 + b^2 r_{2e}^2 - 2abr_{1e}r_{2e}) \tag{B21}$$

To simplify this, we first note that

$$r_{1e}r_{2e} = \frac{l_1^T e}{\|l_1\|\|e\|}\frac{l_2^T e}{\|l_2\|\|e\|} = \frac{l_1^T e e^T l_2}{\|l_1\|\|l_2\|\|e\|^2}, \tag{B22}$$

and because e is a Gaussian random process, when summed over many iterations $E(ee^T) = v^2 I$. $\|e\|$, the Frobenius norm of the error is given

by $E(\|e\|) = \sqrt{Nv^2}$ where N is the total number of MEG channels. Consequently, we can write

$$E(r_{1e}r_{2e}) = \frac{l_1^T l_2}{\|l_1\|\|l_2\|N} = \frac{1}{N}r_{12}. \tag{B23}$$

Next, we examine r_{1e}^2 and note that

$$r_{1e}^2 = \frac{(l_1^T e)^2}{\|l_1\|^2\|e\|^2} \tag{B24}$$

Again we take advantage of the fact that e is a Gaussian random process, so we can write $(l_1^T e)^2 = (\sum_{s=1}^{N}l_{1s}e_s)^2 \approx \sum_{s=1}^{N}(l_{1s}e_s)^2$ because on average the cross terms in the square will sum to zero. Because $E(e_s^2) = v^2$ then $\sum_{s=1}^{N}(l_{1s}e_s)^2 = v^2\sum_{s=1}^{N}(l_{1s})^2 = v^2\|l_1\|^2$. Further, since $E(\|e\|^2) = Nv^2$ we find that

$$E(r_{1e}^2) = \frac{1}{N}. \tag{B25}$$

The same argument can be made to show that

$$E(r_{2e}^2) = \frac{1}{N}. \tag{B26}$$

Substituting Equations B25, B26 and B23 into B21 we see that

$$E_{noise}^2 = \frac{1}{M}\frac{v^2 N}{\|l_1\|^2}\left(Ma^2\frac{1}{N} + Mb^2\frac{1}{N} - M2ab\frac{1}{N}r_{12}\right) \tag{B27}$$

Substituting for a and b this then simplifies to give

$$E_{noise}^2 = \frac{v^2}{\|l_1\|^2}\left(\frac{1 + f_2^2 r_{12}^2 - 2f_2 r_{12}^2}{(1 - f_2 r_{12}^2)^2}\right). \tag{B28}$$

APPENDIX C: Analytical analysis for a dipole fit

For most source reconstruction algorithms, the reconstructed source signal can be written as a weighted sum of sensor measurements, as in Eq. (1). For a dipole fit, the weights are given by

$$w_{d\theta}^T = \frac{l_{d\theta}^T}{l_{d\theta}^T l_{d\theta}}, \tag{C1}$$

i.e. they are a scaled version of the lead field and do not depend on the data covariance – as in a beamformer. To understand how this affects reconstruction error, we can apply these weights to the analytical formulation of the MEG data for the case of 2 sources with random noise (i.e. combine Eq. (8) and Eq. (C1)). Assuming an accurate lead field ($l_{d\theta} \to l_1$) (i.e. source location and orientation have been estimated accurately from the data),

$$\hat{q}_1 = \frac{l_1^T}{l_1^T l_1}l_1 q_1 + \frac{l_1^T}{l_1^T l_1}l_2 q_2 + \frac{l_1^T}{l_1^T l_1}e \tag{C2}$$

Substituting $r_{12} = \frac{l_1^T l_2}{\|l_1\|\|l_2\|}$, we see that

$$\hat{q}_1 = q_1 + \frac{\|l_2\|}{\|l_1\|}r_{12}q_2 + \frac{l_1^T e}{\|l_1\|^2} \tag{C3}$$

Or alternatively

$$\hat{q}_1 = q_1 + \frac{\|l_2\|}{\|l_1\|}r_{12}q_2 + \frac{\|e\|}{\|l_1\|}r_{1e} \tag{C3}$$

Note that the error generated by the contribution of source two to the reconstruction is a linear function of r_{12}, whereas for the beamformer, the equivalent term (δ, Eq. (B1)1) is non-linear. These two functions are shown plotted in Fig. A1, for the case where $\|l_1\| = \|l_2\| = 1 \times 10^{-13}$ T, source amplitudes are 1 nAm and sensor noise takes values of 30, 50 and 100 fT. The nonlinearity in Eq. (B1)1 means that the beamformer is better able to suppress interference from a second source, even if the source topographies are highly correlated. However, this effect is diminished with higher sensor noise.
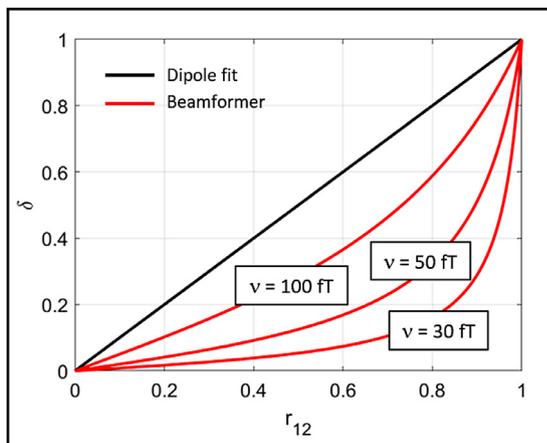
Fig. A1. Projected interference from a second source. Case for a Beamformer in red and a dipole fit in black.

References

Allred, J., Lyman, R., Kornack, T., Romalis, M.V., 2002. High-sensitivity atomic magnetometer unaffected by spin-exchange relaxation. Phys. Rev. Lett. 89 Article Number: 130801.

Baillet, S., 2017. Magnetoencephalography for brain electrophysiology and imaging. Nat. Neurosci. 20, 327–339.

Barratt, E.L., Francis, S.T., Morris, P.G., Brookes, M.J., 2018. Mapping the topological organisation of beta oscillations in motor cortex using MEG. Neuroimage 181, 831–844.

Borna A., Carter T.R., Colombo A.P., Jau Y.-.Y., Berry C., McKay J., Stephen J., Weisend M., Schwindt P.D.D. (2017) A 20-Channel Magnetoencephalography System Based on Optically Pumped Magnetometers. https://arxivorg/ftp/arxiv/papers/1706/170606158pdf.

Borna, A., Carter, T.R., Colombo, A.P., Jau, Y.Y., McKay, J., Weisend, M., Taulu, S., Stephen, J.M., Schwindt, P.D.D., 2020. Non-invasive functional-brain-imaging with an OPM-based magnetoencephalography system. PLoS ONE 15 e0227684.

Boto, E., Bowtell, R.W., Krüger, P., Fromhold, M., Morris, P.G., Meyer, S., Barnes, G.R., Brookes, M.J., 2016. The benefits of atomic magnetometers for MEG: a simulation study. PLoS ONE doi:10.1371/journal.pone.0157655.

Boto, E., Hill, R.M., Rea, R., Holmes, N., Seedat, Z.A., Leggett, J., Shah, V., Osborne, J., Borwtell, R., Brookes, M.J., 2021. Measuring functional connectivity with wearable MEG. Neuroimage 230, 117815.

Boto, E., Holmes, N., Leggett, J., Roberts, G., Shah, V., Meyer, S.S., Duque Muñoz, L., Mullinger, K.J., Tierney, T.M., Bestmann, S., Barnes, G.R., Bowtell, R., Brookes, M.J., 2018. Moving magnetoencephalography towards real-world applications with a wearable system. Nature 555, 657.

Boto, E., Meyer, S.S., Shah, V., Alem, O., Knappe, S., Kruger, P., Fromhold, M., Lim, M., Glover, P.M., Morris, P.G., Bowtell, R., Barnes, G.R., Brookes, M.J., 2017. A new generation of magnetoencephalography: room temperature measurements using optically-pumped magnetometers. Neuroimage 149, 404–414.

Boto, E., Seedat, Z., Holmes, N., Leggett, J., Hill, R.M., Roberts, G., Shah, V., Fromhold, T.M., Mullinger, K.J., Tierney, T.M., Barnes, G.R., Bowtell, R.W., Brookes, M.J., 2019. Wearable Neuroimaging: Combining and Contrasting Magnetoencephalography and Electroencephalography IN SUBMISSION.

Brookes, M.J., Vrba, J., Robinson, S.E., Stevenson, C.M., Peters, A.P., Barnes, G.R., Hillebrand, A., Morris, P.G., 2008. Optimising experimental design for MEG beamformer imaging. NeuroImage 39, 1788–1802.

Cohen, D., 1968. Magnetoencephalography: evidence of magnetic fields produced by alpha-rhythm currents. Science 161, 784–786.

Cohen, D., 1972. Magnetoencephalography: detection of the brain's electrical activity with a superconducting magnetometer. Science 175, 664–666.

Hamalainen, M.S., Hari, R., Ilmoniemi, R.J., Knuutila, J., Lounasma, O.V., 1993. Magnetoencephalography: theory, instrumentation, and applications to non-invasive studies of the working human brain. Rev. Mod. Phys. 65, 413–497.

Haueisen, J., Fleissig, K., Strohmeier, D., Elsarnagawy, T., Huonker, R., Liehr, M., Witte, O.W., 2012. Reconstruction of quasi-radial dipolar activity using three-component magnetic field measurements. Clin. Neurophysiol. 123, 1581–1585.

Hill, R.M., Boto, E., Holmes, N., Hartley, C., Seedat, Z.A., Leggett, J., Roberts, G., Shah, V., Tierney, T.M., Woolrich, M.W., Stagg, C.J., Barnes, G.R., Bowtell, R.R., Slater, R., Brookes, M.J., 2019. A tool for functional brain imaging with lifespan compliance. Nat. Commun. 10.

Hill, R.M., Boto, E., Rea, M., Holmes, N., Leggett, J., Coles, L.A., Papastavrou, M., Everton, S.K., Hunt, B.A.E., Sims, D., Osborne, J., Shah, V., Bowtell, R., Brookes, M.J., 2020. Multi-channel whole-head OPM-MEG: helmet design and a comparison with a conventional system. Neuroimage 219, 116995.

Holmes, M., Leggett, J., Boto, E., Roberts, G., Hill, R.M., Tierney, T.M., Shah, V., Barnes, G.R., Brookes, M.J., Bowtell, R., 2018. A bi-planar coil system for nulling background magnetic fields in scalp mounted magnetoencephalography. Neuroimage 181, 760–774.

Holmes, N., Tierney, T.M., Leggett, J., Boto, E., Mellor, S., Roberts, G., Hill, R.M., Shah, V., Barnes, G.R., Brookes, M.J., Bowtell, R., 2019a. Balanced, bi-planar magnetic field and field gradient coils for field compensation in wearable magnetoencephalography. Sci. Rep. 9.

Holmes, N., Tierney, T.M., Leggett, J., Boto, E., Mellor, S., Roberts, G., Hill, R.M., Shah, V., Barnes, G.R., Brookes, M.J., Bowtell, R., 2019b. Balanced, bi-planar magnetic field and field gradient coils for field compensation in wearable magnetoencephalography. Sci. Rep. 9.

Iivanainen, J., Stenroos, M., Parkkonen, L., 2017. Measuring MEG closer to the brain: performance of on-scalp sensor arrays. Neuroimage 147, 542–553.

Iivanainen, J., Zetter, R., Groen, M., Hakkarainen, K., Parkkonen, L., 2018. On-scalp MEG system utilizing an actively shielded array of optically-pumped magnetometers. bioRxiv, 471391.

Jaklevic, R.C., Lambe, J., Silver, A.H., Mercereau, J.E., 1964. Quantum Interference Effects in Josephson Tunneling. Phys. Rev. Lett. 12, 159–160.

Johnson, C., Schwindt, P.D.D., Weisend, M., 2010. Magnetoencephalography with a two–color pump-probe, fiber-coupled atomic magnetometer. Appl. Phys. Lett. 97.

Johnson, C.N., Schwindt, P.D., Weisend, M., 2013. Multi-sensor magnetoencephalography with atomic magnetometers. Phys. Med. Biol. 58, 6065–6077.

Kamada, K., Sato, D., Ito, Y., Natsukawa, H., Okano, K., Mizutani, N., Kobayashi, T., 2015. Human magnetoencephalogram measurements using newly developed compact module of high-sensitivity atomic magnetometer. Japan. J. Appl. Phys. 54 Article number 026601.

Kominis, I.K., Kornack, T.W., Allred, J.C., Romalis, M.V., 2003. A subfemtotesla multi-channel atomic magnetometer. Nature 422, 596–599.

Mhaskar, R., Knappe, S., Kitching, J., 2012. A low-power, high-sensitivity micromachined optical magnetometer. Appl. Phys. Lett. 101, 241105.

Nurminen, J., Taulu, S., Nenonen, J., Helle, L., Simola, J., Ahonen, A., 2013. Improving MEG performance with additional tangential sensors. IEEE Trans. Biomed. Eng. 60, 2559–2566.

Rampp, S., Stefan, H., Wu, X., Kaltenhäuser, M., Maess, M., Schmitt, F.C., Wolters, C.H., Hamer, H., Kasper, B.S., Schwab, S., Doerfler, A., Blümcke, I., Rössler, K., Buchfelder, M., 2019. Magnetoencephalography for epileptic focus localization in a series of 1000 cases. Brain 142, 3059–3071.

Roberts, G., Holmes, N., Boto, E., Leggett, J., Hill, R.M., Shah, V., Alexander, N., Maguire, E., Kessler, K., Beebe, S., Fromhold, M., Barnes, G.R., Bowtell, R., Brookes, M.J., 2019. Towards OPM-MEG in a virtual reality environment. Neuroimage 199, 408–417.

Robinson S., Vrba J. (1998) Functional neuroimaging by synthetic aperture magnetometry. In Recent Advances in Biomagnetism, ed Yoshimoto T, Kotani M, Kuriki S, Karibe H, Nakasato N, Tohoku Univ Press, Sendai, Japan 302–305.

Sander, T.H., Preusser, J., Mhaskar, R., Kitching, J., Trahms, L., Knappe, S., 2012. Magnetoencephalography with a chip-scale atomic magnetometer. Biomed. Opt. Express 3, 981–990.

Sarvas, J., 1987. Basic mathematical and electromagnetic concepts of the biomagnetic inverse problem. Phys. Med. Biol. 32, 11–22.

Shah, V., Romalis, M.V., 2009. Spin-exchange-relaxation-free magnetometrty using elliptically polarised light. Phys. Rev. A 80, 013416.

Shah, V.K., Wakai, R.T., 2013. A compact, high performance atomic magnetometer for biomedical applications. Phys. Med. Biol. 58, 8153–8161.

Sheng, D., Perry, A.R., Krzyzewski, P., Geller, S., Kitching, J., Knappe, S., 2017. A microfabricated optically-pumped magnetic gradiometer. Appl. Phys. Lett. 110, 031106.

Stenroos, M., Hunold, A., Haueisen, J., 2014. Comparison of three-shell and simplified volume conductor models in magnetoencephalography. Neuroimage 94, 337–348.

Taulu, S., Simola, J., 2006. Spatiotemporal signal space separation method for rejecting nearby interference in MEG measurements. Phys. Med. Biol. 51, 1759.

Tierney, T.M., Holmes, N., Mellor, S., López, J.D., Roberts, G., Hill, R.M., Boto, E., Leggett, J., Shah, V., Brookes, M.J., Bowtell, R., Barnes, G.R., 2019. Optically pumped magnetometers: From quantum origins to multi-channel magnetoencephalography. Neuroimage 199, 598–608.

Van Uitert, R., Weinstein, D., Johnson, C., 2003. Volume currents in forward and inverse magnetoencephalographic simulations using realistic head models. Ann. Biomed. Eng. 31, 21–31.

Vrba, J., Robinson, S., 2001. Signal processing in magnetoencephalography. Methods 25, 249–271.

Xia, H., Baranga, A.B.A., Hoffman, D., Romalis, M.V., 2006. Magnetoencephalography with an atomic magnetometer. Appl. Phys. Lett. 89.

Zimmerman, J.E., Theine, P., Harding, J.T., 1970. Design and operation of stable rf-biased superconducting point-contact quantum devices. J. Appl. Phys. 41, 1572–1580.